50th AIAA Aerospace Sciences Meeting including the New Horizons Forum and Aerospace Exposition
09 - 12 January 2012, Nashville, Tennessee
AIAA 2012-0947

Dual-Mode Scramjet Combustor: Numerical Sensitivity and Evaluation of Experiments

Ryan T. Milligan[*], Jiwen Liu[†] and Chung-Jen Tam[‡]
Taitech, Inc., Beavercreek, OH 45430
Dean R. Eklund[§], Mark A. Hagenmaier[**], Douglas L. Davis[††], Daniel J. Risha[‡‡] and Mark Gruber[§§]
AFRL, WPAFB, OH 45433
and
Tarun Mathur[***]
Innovative Scientific Solutions, Inc., Dayton, OH 45440

Experiments were performed at the Air Force Research Laboratory's Propulsion Directorate (AFRL/RZ) in Research Cell 22 (RC22). Twelve cases from the experiment were computationally analyzed and each case varied in either engine operating condition and/or combustor configuration. Initial computations were performed on all twelve cases to establish a baseline computational approach. Computations were performed on one of the cases to test sensitivity to turbulent Schmidt number, reaction rate, and grid resolution. Improvements to the baseline analysis using the results from the sensitivity analyses were extended to two additional cases. It was shown that adjustments in Schmidt number, reaction rate, or grid refinement improved the agreement with experimental data for two cases relative to the baseline results, but worsened agreement for the third case. It was left undetermined that grid refinement was a better approach to improving the baseline analysis as compared to calibrations in Schmidt number and/or reaction rate. Improvement to the grid using local refinement in regions with chemical reactions produced better results for one case and was computationally less expensive than globally refining the grid. Negligible differences were shown between results that were obtained using wall functions with Y+ value as high as 38 or results obtained using wall integration with Y+ values around one. Negligible differences were shown between periodic results that were obtained by averaging results using either a constant CFL or a constant time step. CFL-averaging a result using the constant CFL approach was 5.4 times less computationally expensive than using the constant time step approach. Computations showed that 2.53-lbm/sec. of air leaked into the exhauster housing at the exit of the combustor in RC22's test apparatus.

I. Introduction

Previous experimental efforts in RC22 have studied combustion in rectangular flowpaths.[1] Efforts in RC22 have recently investigated circular ("axisymmetric" or "round") combustors. Circulator combustors, for the same cross-sectional area eliminate the challenges involved with corner-flow effects and have reduced weight. On the other hand, circular combustors pose challenges which involve effective fuel penetration and flame propagation.

[*] Research Engineer, Taitech, Inc., Beavercreek, OH, Member AIAA.
[†] Research Engineer, Taitech, Inc., Beavercreek, OH, Associate Fellow AIAA.
[‡] Research Engineer, Taitech, Inc., Beavercreek, OH, Associate Fellow AIAA.
[§] Aerospace Engineer, Aerospace Propulsion Division, 1950 Fifth St, Senior Member AIAA.
[**] Aerospace Engineer, Aerospace Propulsion Division, 1950 Fifth St, Senior Member AIAA.
[††] Aerospace Engineer, Aerospace Propulsion Division, 1950 Fifth St, Senior Member AIAA.
[‡‡] Aerospace Engineer, Aerospace Propulsion Division, 1950 Fifth St, Associate Fellow AIAA.
[§§] Aerospace Engineer, Aerospace Propulsion Division, 1950 Fifth St, Associate Fellow AIAA.
[***] Research Engineer, Innovative Scientific Solutions, Inc., Dayton, OH, Senior Member AIAA.

Report Documentation Page

Form Approved
OMB No. 0704-0188

1. REPORT DATE	2. REPORT TYPE	3. DATES COVERED
JAN 2012		**00-00-2012 to 00-00-2012**

4. TITLE AND SUBTITLE	5a. CONTRACT NUMBER
Dual-Mode Scramjet Combustor: Numerical Sensitivity and Evaluation of Experiments	5b. GRANT NUMBER
	5c. PROGRAM ELEMENT NUMBER
6. AUTHOR(S)	5d. PROJECT NUMBER
	5e. TASK NUMBER
	5f. WORK UNIT NUMBER
7. PERFORMING ORGANIZATION NAME(S) AND ADDRESS(ES) **Air Force Research Laboratory,Aerospace Propulsion Division,1950 Fifth St,Wright Patterson AFB,OH,45433**	8. PERFORMING ORGANIZATION REPORT NUMBER
9. SPONSORING/MONITORING AGENCY NAME(S) AND ADDRESS(ES)	10. SPONSOR/MONITOR'S ACRONYM(S)
	11. SPONSOR/MONITOR'S REPORT NUMBER(S)

12. DISTRIBUTION/AVAILABILITY STATEMENT
Approved for public release; distribution unlimited

13. SUPPLEMENTARY NOTES

14. ABSTRACT

15. SUBJECT TERMS

16. SECURITY CLASSIFICATION OF:			17. LIMITATION OF ABSTRACT	18. NUMBER OF PAGES	19a. NAME OF RESPONSIBLE PERSON
a. REPORT **unclassified**	b. ABSTRACT **unclassified**	c. THIS PAGE **unclassified**	**Same as Report (SAR)**	**33**	

The Reynolds-Averaged-Navier-Stokes (RANS) approach was used in this Computational Fluid Dynamics (CFD) analysis. The RANS approach poses challenges for accurately predicting the amount of air/fuel mixing, which affects combustion. Other approaches such as Large-Eddy Simulation (LES) and Direct-Numerical Simulation (DNS) are too computationally expensive to perform a study of the magnitude shown in this analysis, but could possibly be used in a future study on one of the twelve cases. The dominant mass transport mechanism in a RANS analysis is the turbulent Schmidt number, which is defined as the ratio of the turbulent transport of momentum to mass. In this analysis a constant value of turbulent Schmidt number was used to describe the overall mixing characteristics of the flow-field. Using this method to characterize a flow-field is often limited to a model calibration, but it has been shown that after initial calibration the constant value of turbulent Schmidt number can provide predictive capability within a limited range of engine operation.[2] Computational modeling of the HiFIRE Flight 2 tests using a constant turbulent Schmidt number has also been successful.[3] There are limitations and challenges with regard to the constant turbulent Schmidt number approach. The turbulent Schmidt number in the presence of species gradients and shear layers is known to vary.[4] It is also expected that significant changes to an engine configuration may require a re-calibration of turbulent Schmidt number in order to acceptably predict engine operation. Other factors explored in this analysis that contribute to accurate prediction are the kinetics model and grid resolution.

II. Experimental Setup

RC22 is presently configured as a supersonic wind tunnel facility with a direct-connect nozzle and has been testing undistorted ethylene-based combustion in circular combustors. Two facility nozzles, a Mach 1.8 and Mach 2.2, are used to simulate flight conditions ranging from Mach 3.0 to Mach 5.0. The nozzles are designed using the method of characteristics with boundary layer correction to provide an average Mach number of either 1.8 or 2.2 to the test section. Flight enthalpies greater than Mach 3.0 are achieved using a natural-gas vitiator. The test section consists of a facility nozzle, isolator, and combustor. The isolator has a 0.25° divergence angle and was used for all combustion experiments described in this analysis.[5] Two combustor configurations were analyzed; the first was a fully divergent combustor; the second configuration used a constant area section with step. Figure 1 shows a flow-path schematic of one of the configurations. Figure 2 shows an outline of the two configurations that were examined in this analysis and the differences between each configuration are marked in sections C3 and C4.

RC22 has several measurements that can be provided for purposes of model evaluation. Static wall pressure measurements and subsurface thermocouple measurements are acquired along the axial length of the test section and around the circular geometry at three circumferential locations (0°, 120°, and 240°). In-stream Pitot probes at the exit of the combustor can be rotated to assess symmetry.[6] The entire test rig sits on a thrust stand for load-cell based measurements. Water cooling of all components permits long-duration, steady state testing. Bulk heat loss is measured from each water-cooled component. There are two isolator components I1 and I2; there are 5 combustor sections C1-C5 (see Figure 2). Stream thrust and combustion efficiency are deduced from a load-cell force, in conjunction with base and exit pressures, wall pressure, and component-heat-loss data.[7] Each combustor configuration has a circular cavity and three axial stations for fuel injection. There are eight equally spaced flush-wall fuel injectors at each axial station. The primary injectors are upstream of the cavity and are at a 30° angle to the wall, the secondary injectors are downstream of the cavity, offset circumferentially with respect to the primary injectors, and are normal to the wall. In the cavity, there are eight normal injectors which are in-line with the primary injectors. The cavity injectors are designed to assist and stabilize cavity flames, but are not typically used as a primary fueling source. Figure 2 outlines both configurations; note the axial locations of the injectors and recall that the secondary injectors are offset with respect to the primary injectors. The Pitot probe section (PRB) is not physically bolted to the C5-exit flange. A small air gap around the C5 exit prior to the exhaust nozzle allows the test stand to float for purposes of measuring load-cell force. A computational analysis investigating the air gap was performed and is shown in a later section of the analysis. The optical calibrator section (OC) is constant area and is used to calibrate the nozzle, it is not considered part of the isolator (isolator begins at X=0.0-in, which is downstream of the OC section).

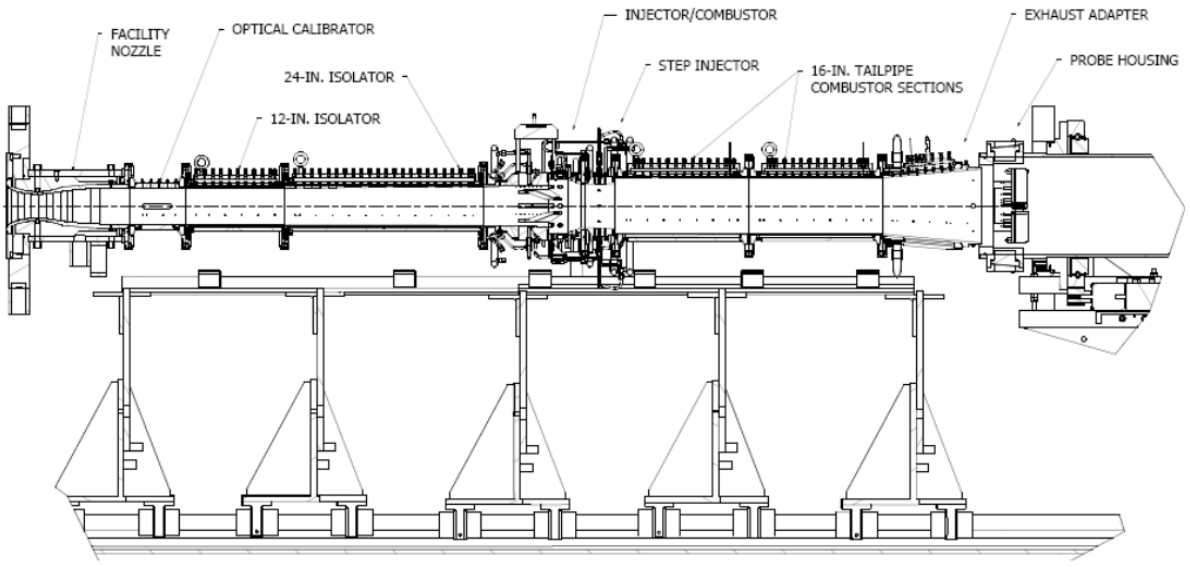

Figure 1. Flowpath schematic

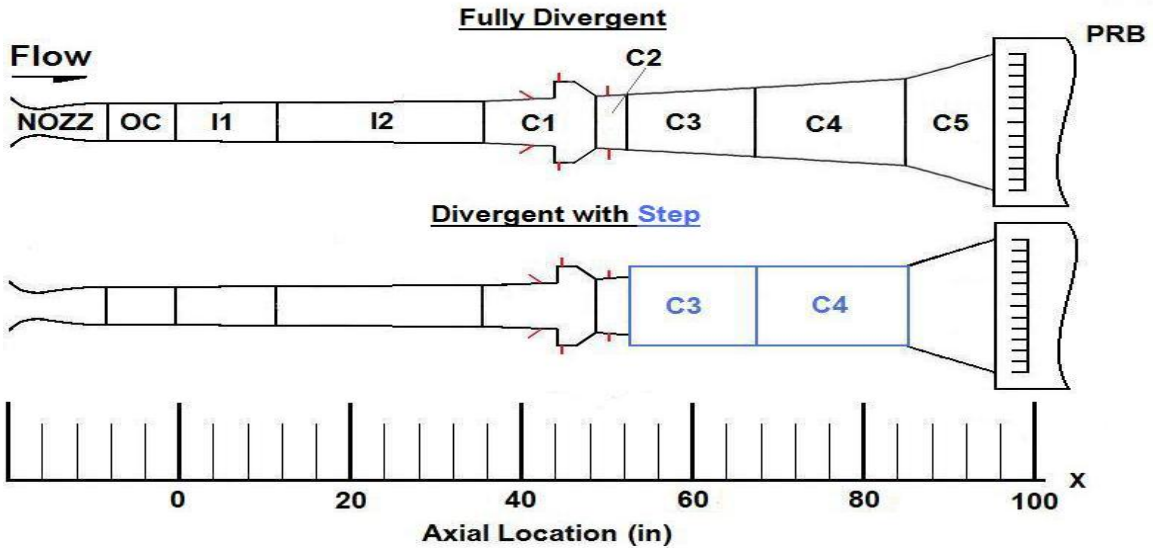

Figure 2. Fully divergent isolator/combustor (top) and combustor with step (bottom)

Characterizing an experimental facility using CFD requires knowledge of the uncertainties associated with the experimental data. The parameters by which the CFD is compared to in this analysis are static-wall pressure distribution, combustor-exit-Pitot-pressure distribution, bulk-heat loss, Δ-stream thrust, and combustion efficiency; the measurement uncertainties are $\sigma_{p_m} = \pm 0.30\%$, $\sigma_{Pp_m} = \pm 1.0\%$, $\sigma_{q_m} = \pm 5.0\%$, $\sigma_{\Delta ST_m} = \pm 1.0\%$, and $\sigma_{\eta_m} = \pm 4.0\%$, respectively.[7] Δ-stream thrust and combustion efficiency are defined in the Baseline Results Section. The experimental data is based upon steady state combustor operation. Data were collected at 1-Hz or every second of operation. At steady state, ten seconds of experimental data (for all twelve cases) were analyzed for assessing operational unsteadiness. The standard deviation was determined for each parameter; the standard deviation in this calculation was used as a measure of uncertainty for operational unsteadiness and Equation 1 shows the formulation using combustion efficiency, η, as an example. Using the example, the total uncertainty in this analysis is based on the sum of squares of measurement uncertainty and the uncertainty associated with operational unsteadiness, which is shown in Equation 2. In this analysis comparisons would be considered acceptable if CFD results fell within the bounds of the total experimental uncertainty. The level of operational unsteadiness and its uncertainty usually varies on a case-by-case basis but, for simplicity, the uncertainty for a given parameter was

averaged over all twelve cases, which is shown in Equation 3. Computational uncertainties were not accounted for in this analysis.

$$\sigma_{\eta_o} = \sqrt{\frac{1}{N-1}\sum_k^N (\eta_k - \bar{\eta})^2} \quad [1]$$

$$\bar{\sigma}_\eta = \sqrt{{\sigma_{\eta_m}}^2 + {\bar{\sigma}_{\eta_o}}^2} \quad [2]$$

$$\bar{\sigma}_{\eta_o} = \frac{\sum_k^N \sigma_{\eta_o}}{N} \quad [3]$$

The average-total uncertainty for static-wall pressure, combustor-exit-Pitot pressure, bulk heat loss, Δ-stream thrust, and combustion efficiency are $\bar{\sigma}_p = \pm 1.70\%$, $\bar{\sigma}_{Pp} = \pm 1.1\%$, $\bar{\sigma}_q = \pm 5.3\%$, $\bar{\sigma}_{\Delta ST} = \pm 1.0\%$, and $\pm \bar{\sigma}_\eta = \pm 4.1\%$. The level of operational unsteadiness had a minimal contribution to the average-total uncertainty for any given parameter, except pressure. All experimental pressure and combustor-exit-Pitot pressure distributions shown in the figures throughout this analysis include all measured values for each data set over ten seconds of steady state operation.

III. Methodology

The objective in this analysis is to improve the baseline analysis by testing computational sensitivities using the RANS approach. The data provided includes twelve cases from the experiment. Initially, a baseline computational approach was established using a baseline grid. Stemming from the baseline was a series of sensitivity analyses performed on one of the original twelve cases. The primary sensitivities found were those to turbulent Schmidt number, reaction rate, and grid resolution. Sensitivities to the analysis were extended to two additional cases to test the broader effectiveness of the sensitivity. The practices and procedures established in this analysis will help guide future CFD work involving RC22.

The twelve cases that were examined in this analysis were chosen based upon a range of combustor operation, range including fuel splits, high and low combustor equivalence ratios (Φ), two flight conditions, and two combustor configurations. Table 1 summarizes the conditions for the twelve cases chosen for this analysis; each case is individually identified using the "Case Identifier." The isolator entrance Mach numbers and enthalpies applied to the facility nozzles were deduced via a correlation which relates the facility configurations to those that would be used in a flight configuration.[8]

Table 1. Summary of conditions

Case Identifier	M (isolator entrance)	Config.	P_{dyn} (lb/ft^2)	T_o (R)	P_o (psi.)	Φ (total)	Φ (primary)	Φ (cavity)	Φ (secondary)
F09022BN	2.2	div.	1000	2206	104.6	0.90	0.90	-	-
F09062BI	2.2	div.	1000	2200	104.5	0.90	0.32	-	0.58
F09062BS	2.2	div.	1000	2202	105.5	0.30	0.30	-	-
F09119AW	2.2	step	1000	2201	105.6	0.89	0.89	-	-
F09128AT	2.2	step	1000	2199	105.2	0.91	0.31	-	0.60
F09119BF	2.2	step	1000	2200	105.5	0.30	0.30	-	-
F09246AE	1.8	div.	1000	1500	55.1	0.89	0.70	0.19	-
F09260AH	1.8	div.	1000	1498	54.8	0.92	0.27	0.04	0.62
F09260AY	1.8	div.	1000	1500	55.1	0.30	0.30	-	-
F09175AD	1.8	step	1000	1502	55.5	0.90	0.90	-	-
F09194AF	1.8	step	1000	1503	55.0	0.89	0.30	-	0.59
F09175AK	1.8	step	1000	1498	54.7	0.30	0.30	-	-

An interesting phenomenon was observed at the low-Φ condition for case F09119BF compared to case F09119BE (not part of the twelve cases) which was operating under the exact same conditions. Figure 3 shows wall pressure (left) and Pitot pressure (right) for these two cases.

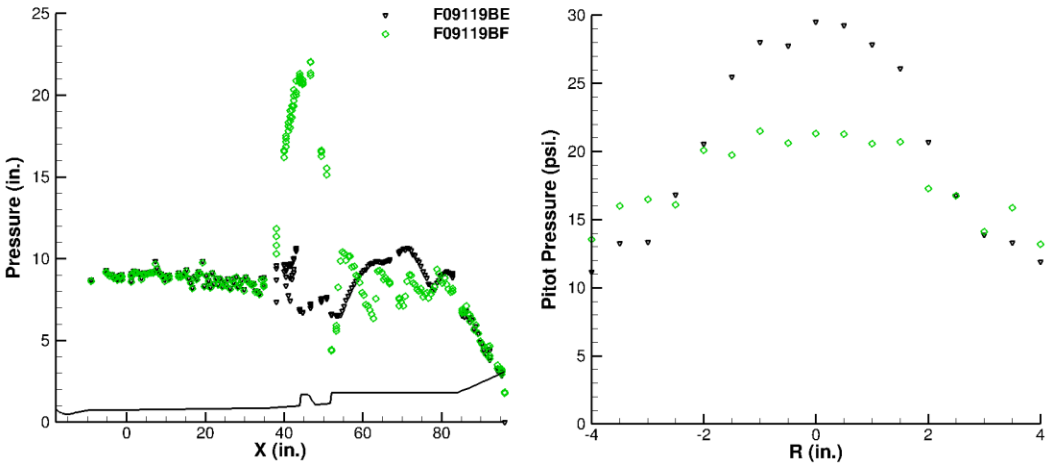

Figure 3. Bi-modal engine operation; wall pressure (left) Pitot pressure (right)

The peak pressure in case F09119BF is 120% greater than that in case F09119BE, and was further upstream. The pressure distribution for case F09119BF suggests that is was operating in dual-mode with a small upstream shock train and a portion of the flow subsonic around the region of the cavity. Little burning was observed in the step region of the flow for this case. Case F09119BE shows no shock-train development ahead of the cavity and shows most of its burning occurring in the constant-area section of the combustor. This type of pressure distribution possibly suggests that this case was operating in pure-scramjet mode. The Pitot distribution for this case shows less uniform properties near the core of the combustor where Pitot pressure peaks. The performance between the two cases is comparable in spite of the extreme differences in the pressure distributions. The performance and heat loss between the two cases is tabulated in Table 2.

Table 2. Bi-modal engine operation; performance and heat loss

	Δ-stream thrust (lb_f)	**η**	**Iso. heat loss (Btu/s)**	**Comb. heat Loss (Btu/s)**
F09119BF	181	0.85	131	416
F09119BE	169	0.78	131	365

The best explanation for the phenomena has to do with the cold start method the experimentalists use. Spark plugs located in the cavity as well as an air throttle are often used to ignite the combustor. Typical practice is to ignite the flow with spark plug only, but at times air throttle assistance is needed. Case F09119BF needed the assistance of the air-throttle to ignite. The air throttle supplies additional air-mass flow which creates an aerodynamic blockage. This blockage helps establish a pre-combustion-shock train ahead of the combustor which increases pressure, slows down the flow, and aids in the ignition of the flow. Once the flow ignites the air throttle valve is closed and the combustor operates until it achieves steady state. Case F09119BE did not need the assistance of the air throttle; this case did not need the air throttle because it was run later during the day of testing and the facility was hot. Experimentalists tested several cases between the two configurations to test the sensitivity to the air throttle and it was determined that the only type of engine condition sensitive to the bi-modal operation were cases that operated using the Mach=2.2 nozzle, at low Φ, and using the step configuration. None of the other remaining eleven cases were sensitive to the cold start methods or time of day.

The purpose of this short discussion is to underline the importance of scrutinizing experimental data in order to understand and make an accurate assessment. The numerical modeling in this analysis simply used a 3-step kinetics mechanism to ignite the flow prior to the primary mechanism and did not model an ignition source or air throttle. The 3-step mechanism used artificially high reaction rates to ignite the flow; hence the mechanism itself is not discussed. The predicted (CFD) results were reminiscent of case F09119BF which is why it was chosen as one of the twelve cases rather than case F09119BE. A future study might be performed to better understand the bi-modal operation between these two cases, but the modeling methods in this analysis were not sufficient for that type of analysis.

IV. Computational Approach

A summary of the baseline computational procedures used in this analysis is outlined in Table 3. Any variation from these baseline procedures are outlined in the first paragraph of each section throughout the analysis. Many of the variations from the baseline analysis are performed for purposes of analyzing solution sensitivity.

Table 3. Summary of baseline numerics

Numeric	Baseline	Notes
Grid	Structured	Gridgen v15
Solver	CFD++ 10.1.1	Metacomp Technologies, Ref. 9
CFD type	RANS	Reynolds-Averaged Navier Stokes
Turbulence Model	2-eqn. cubic k-ε	Ref. 10
Schmidt Turbulent	0.5	Controls turbulent transport of mass
Prandtl Turbulent	0.9	Controls turbulent transport of energy
Kinetics Model	TP2 (Princeton Model)	22-species ethylene combustion, Ref. 11
Simulation type	Steady state	CFL=5.0
Inviscid order	2nd	
Limiter	Minmod	
Rieman dissipation	LHS only	Minimum computational dissipation
Wall functions	Adv. Two-layer	Has a built-in wall-integration switching function
Heat Transfer	1D-Resistive Layer	Treats impediments to heat transfer like resistors

The grid for the baseline analysis was a 3D structured grid which used a symmetry assumption. This type of grid is called a sector grid and was comprised of 1/16th of the overall RC22 experimental geometry. The sector grid allows for increased grid resolution without the computational expense of modeling the entire geometry. This type of grid may not be sufficient to analyze asymmetric flow-fields because only 1/16th of the overall geometry is modeled, but the experimental data in this analysis has shown that all twelve cases exhibited highly symmetric flow-fields.[12] The overall grid size using hexahedral cells for the divergent and step configurations was ~2,000,000 and ~2,200,000 cells, respectively. The discrepancy in size is due to the additional cells needed to fill the constant area region of the step combustor. The average stretching ratio for each grid was 1.05 and the maximum stretching ratio was 1.2. Maximum Y+ values for cases using the Mach = 1.8 and Mach = 2.2 facility nozzles was 38 and 50, respectively. CFD++ uses a switching function that automatically integrates to the wall in regions where Y+ values are around one; often, low-speed recirculation zones (such as cavity flows) had Y+ values around one. The wall-time per iteration was approximately 6.5-seconds when using the TP2 kinetics model at a CFL=5 and using 128 processors. Figure 4 shows the boundaries used for the analysis; the fully divergent configuration was used as the example. The secondary injector's were 22.5° offset with respect to the primary and cavity injectors.

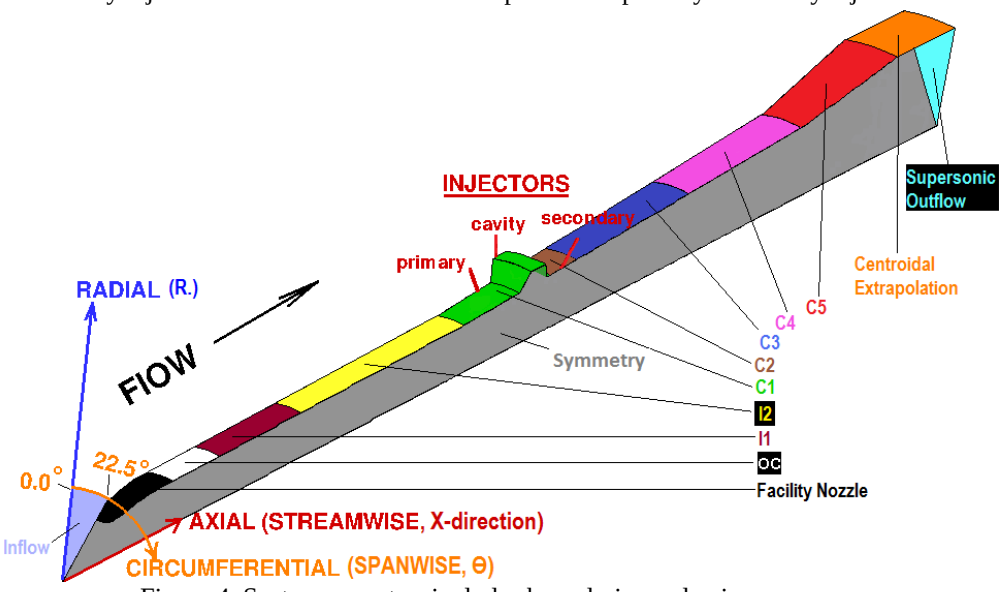

Figure 4. Sector geometry, includes boundaries and axis names

The inflow condition was set to the total (stagnation) conditions for the appropriate nozzle type for each case. The wall boundary conditions from facility nozzle to C5 used a resistive-layer-heat-transfer model for heat loss. The resistive-layer-heat-transfer model used the average-wall thicknesses, material properties, and a backside water cooling temperature as inputs from the experiment which was around room temperature (540-R). The injectors used a mass-flow rate and static-temperature condition as inputs from the experiment. The symmetry boundary condition was used on the side faces of the sector geometry. A centroidal extrapolation condition was used downstream of the exit of the combustor, neglecting the effects of the Pitot housing geometry downstream of the combustor exit. Lastly, a supersonic outflow condition was used which required no addition inputs. Table 4 summarizes the resistive-layer-heat transfer properties used in the analysis. The thermal conductivities for copper, 316-stainless steel, and 4140-precipitated-stainless steel were 226.0, 9.4, and 27.0-Btu/hr-ft-R, respectively. The thermal conductivity for the thermal barrier coating (TBC) was 0.5-Btu/hr-ft-R.

Table 4. Wall properties for heat transfer

	Substrate Material		**Coating**	
Component	**Material**	**Thickness**	**Material**	**Thickness**
		(in.)		**(in.)**
NZ	copper	0.3682	None	0.0000
OC	316	0.1000	None	0.0000
I1	316	0.1000	None	0.0000
I2	316	0.1000	None	0.0000
C1	4140	0.1000	TBC	0.0200
C2	4140	0.1000	TBC	0.0200
C3	316	0.1000	TBC	0.0200
C4	316	0.1000	TBC	0.0200
C5	316	0.1000	TBC	0.0200

V. Baseline Results

This section provides baseline results using the baseline grid and baseline numerics. Baseline results for case F09175AK compare five key parameters to the experimental data for purposes of determining the predictive capability of the model. As mentioned in a previous section, the five parameters are combustor-pressure distribution, combustor-exit-Pitot pressure, Δ-stream thrust, combustion efficiency, and heat loss. Figure 5 shows baseline predicted results and experimental data for case F09175AK, which operated at a low Φ (primary only fuel injection) using the M=1.8 nozzle and the step configuration.

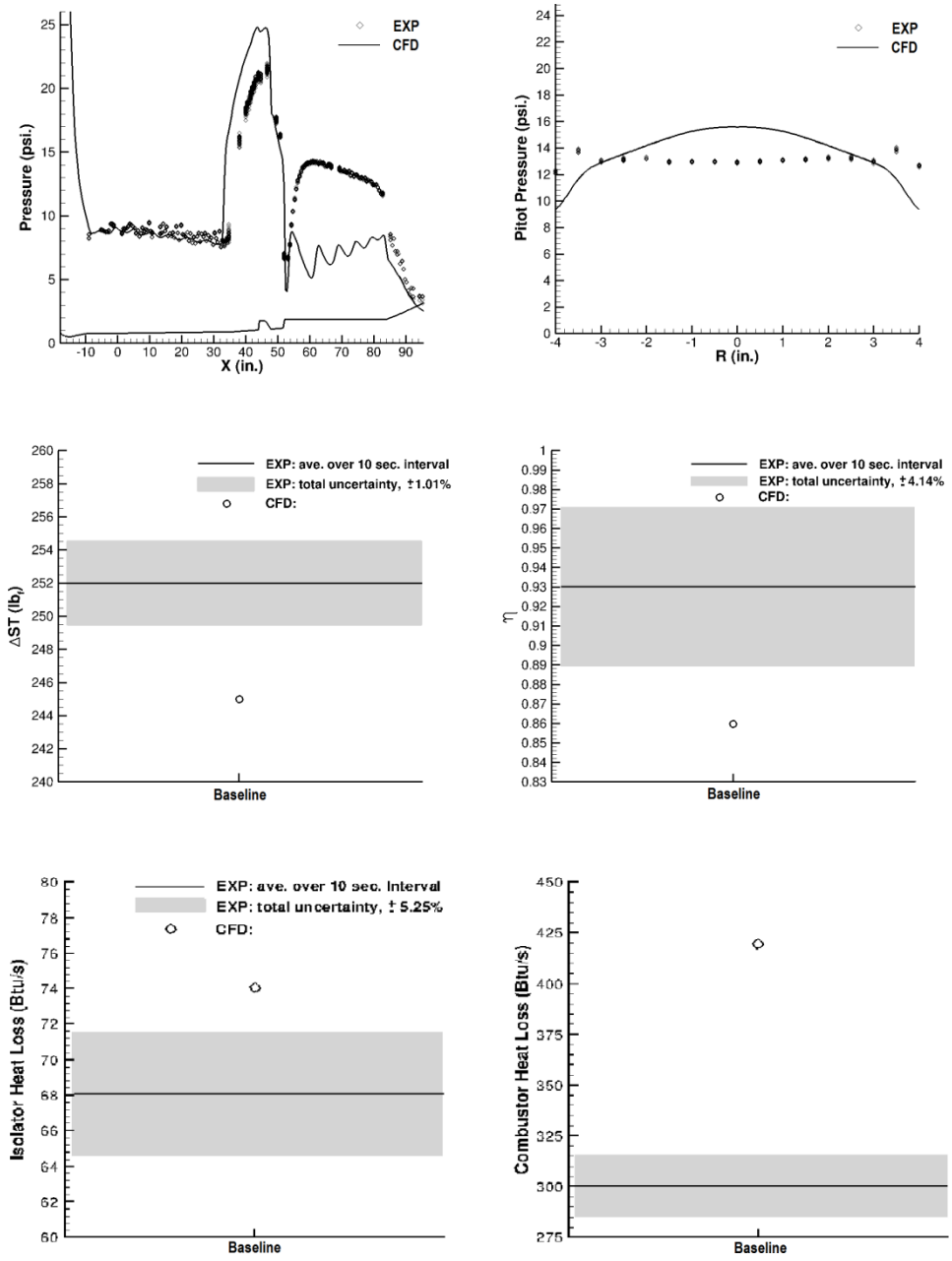

Figure 5. The 5 predicted parameters and the experiment for case F09175AK

With reference to Figure 5, wall pressure (top left) shows that the model over-predicted peak combustor pressure by 3-psia or 14% as compared to the experiment. The over-predicted shock position was 2-in. further upstream as compared to the experiment and the model did not predict a secondary pressure rise in the constant area section of the combustor. Pitot pressure (top right) shows that the predicted properties were less uniform than the experiment, which resulted in an over-prediction of core Pitot pressure (R = 0.0-in.) by 20%. The model under-predicted Δ-stream thrust and combustion efficiency by 2.8% and 7.0%, respectively. Isolator and combustor heat loss were over-predicted by 8.8% and 39.3%, respectively.

Figure 6 is a prediction summary for all of the twelve cases including F09175AK. The purpose of this summary is to help analyze and evaluate each prediction from a "big picture" perspective. The nominal value is equal to zero in every case because it is the experimental value subtracted by itself. The grey area is the total experimental uncertainty for a given parameter. Percentages are the predicted value subtracted by the experimental value then

divided by the experimental value and multiplied by 100%. Equations 4-6 show a verbose description of the formulations. The shock position is not expressed as a percentage; rather, it is expressed as an absolute difference in inches. Note the purpose of the negative sign in Equation 5 is to reverse the polarity of the X-axis in order to reference position relative to the peak pressure inside the combustor rather than the isolator entrance which rests at X=0.0-in. This also helps maintain consistency that a positive value indicates an over-prediction and a negative value indicates an under-prediction. For example, using the wall pressure distribution from Figure 5 (top left) shows the CFD over-predicted peak pressure, but it could be counter intuitive to say that the CFD under-predicted shock position if not for the negative sign.

$$\text{nominal} = 0 = \exp - \exp \quad [4]$$

$$\text{shock position} = -(\text{CFD} - \exp) \quad [5]$$

$$\text{percentage} = \frac{\text{CFD} - \exp}{\exp} \times 100\% \quad [6]$$

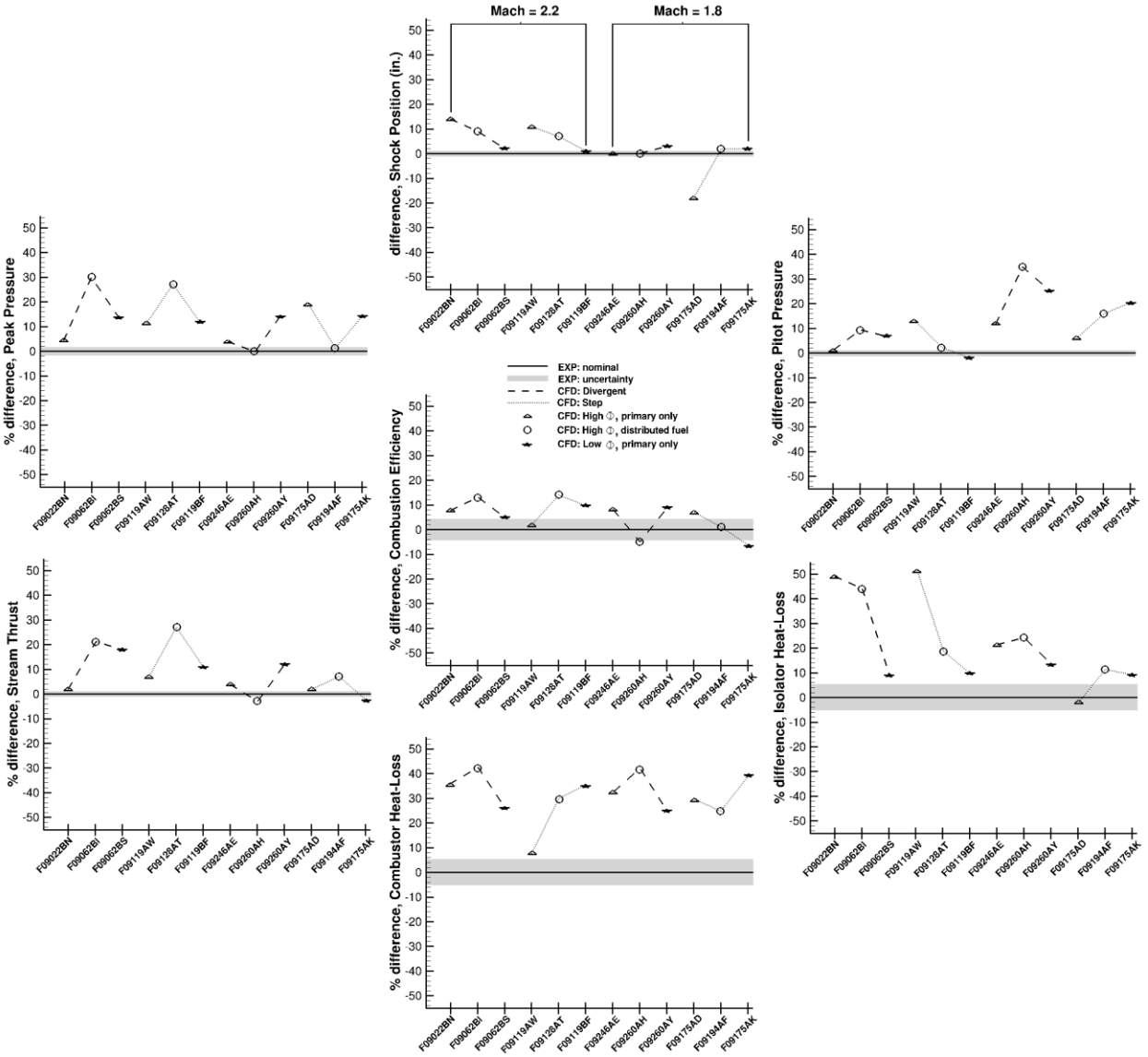

Figure 6. Prediction summary for all twelve cases

Shock Position (top)

Both configurations operating with the M=2.2 nozzle behaved similarly for the same Φ. At a high Φ and primary injection only the shock position was over-predicted (further upstream) by more than 10-in. At a high Φ with distributed fueling the shock position was over-predicted by 10-in. or less. At a low Φ the shock position was only over-predicted by 1- and 2-in. Shock position for cases operating with the M=1.8 nozzle behaved differently. Five of the six cases either predicted shock position within the range of experimental uncertainty or over-predicted by a marginal 2- and 3-in. Case F09175AD was the only case to under-predict shock position and that is explained below.

Peak Pressure (top left)

Cases operating with the M=2.2 nozzle at a high Φ with distributed fuel over-predicted peak pressure by as much as 30%. This was in contrast to cases operating with the M=1.8 nozzle, which for distributed fueling, were able to predict peak pressure within the range of experimental uncertainty.

Pitot Pressure (top right)

Cases operating with the M=1.8 nozzle over-predicted core-Pitot pressure by as much as 35%. Three out of the six cases operating with the M=2.2 nozzle predicted core-Pitot pressure near the range of experimental uncertainty, although five out of six were over-predicted.

Combustion Efficiency (middle)

Cases which operated using the M=2.2 nozzle at a high Φ with distributed fuel over-predicted combustion efficiency by more than 10%. Two of the six cases operating using the M=1.8 nozzle fell within the range of experimental uncertainty. Equation 7 shows the enthalpy based method for computing combustion efficiency from the computational results. The combustion efficiency is defined in equation 7, where Y_i is the computed species mass fraction and $Y_{i,ideal}$ is the ideal-species composition obtained from a chemical equilibrium calculation using the one-dimensional static enthalpy and pressure. Note that T_{ref} denotes the computed non-reacting, isolator-entrance static temperature, and h signifies the static enthalpy. The reference species composition is set to the composition exiting the OC section as determined experimentally from the measured flow rate, static pressure, heat loss, and area assuming chemical equilibrium.

$$\eta = \frac{h(T_{ref},Y_i) - h(T_{ref},Y_{ref})}{h(T_{ref},Y_{i,ideal}) - h(T_{ref},Y_{ref})} \quad [7]$$

Δ-Stream Thrust (bottom left)

Cases operating with the M=2.2 nozzle and distributed fuel over-predicted Δ-stream thrust by as much as 27%. Cases operating using the M=1.8 nozzle had much better predictions, but two cases under-predicted Δ-stream thrust. Equation 8 shows the Δ-stream thrust calculation, which is the difference in stream thrust at the exit of the combustor (x=96-in.) and the isolator entrance (x=0.0-in.). $\dot{m}$ is the mass-flow rate, $\bar{u}$ is the average velocity, $\bar{p}$ is the average static pressure, and A is the area.

$$\Delta ST = (ST_{@\ 96.0"} - ST_{@\ 0.0"}) = (\dot{m}\bar{u} + \bar{p}A)_{@\ 96.0"} - (\dot{m}\bar{u} + \bar{p}A)_{@\ 0.0"} \quad [8]$$

Isolator Heat Loss (bottom right)

Eleven of the twelve cases over-predicted isolator heat loss. Cases operating with the M=2.2 nozzle over-predicted isolator heat loss by as much as 50%. Cases at low Φ had slightly better isolator heat loss predictions. F09175AD, which under-predicted shock position, was the only case to under-predict isolator heat loss.

Combustor Heat Loss (bottom)

All cases, with the exception of F09119AW, over-predicted combustor-heat loss between 25% and 45%.

Prediction Trends

As expected, cases which over-predicted peak pressure were also more likely to over-predict combustion efficiency, Δ-stream thrust, and shock position. Cases which had reasonable predictions in terms of shock position, peak pressure, combustion efficiency and Δ-stream thrust were most likely to have poor Pitot pressure prediction which was not expected. Cases that had the best shock position prediction also had better isolator heat loss prediction than cases that over-predicted shock position. This suggests that a baseline turbulent Prandtl number of 0.9 was a reasonably good choice for non-reacting isolator flow, given the shock position was in reasonable agreement with the experiment. It is possible that turbulent Prandtl number of 0.9 will need adjustment for the combustor flow where chemical reactions and strong temperature gradients exist, although other factors such as radiation effects and water-side-convective-heat transfer resistivity were not accounted for in the heat-transfer analysis.

Possible Improvements: Pros and Cons

The cases which used the M=2.2 nozzle all appear to suffer from too much upstream heat release, which seems to cause over-predictions in peak pressure, shock position, and Δ-stream thrust. Conventional practice would be to limit/delay heat release to obtain an improved prediction. This can be achieved in two ways: increasing turbulent Schmidt number to reduce mixing and/or cutting reaction rates from the kinetics model to delay combustion. Both methods would effectively shift combustion downstream. These methods may improve predictions for cases using the M=2.2 nozzle, but could prove detrimental for predictions which used the M=1.8 nozzle. This is because some of the predictions using the M=1.8 nozzle had reasonably good agreement with the experiment using baseline values for turbulent Schmidt number and reaction rate. Further grid refinement may be necessary in certain reacting regions of the flow to improve agreement as well.

Under-predicted Shock Position

Case F09175AD, which used the step configuration, was the only case that appeared to under-predict shock position. This was also the only case in which the CFD predicted lean-cavity blowout, but the flame sustained itself in the step region of the combustor. The lean-cavity blowout was the result of a decoupling between the cavity and the fuel stream. In the experiment this case's cavity did not blow out. This underlines some of the shortcomings in the baseline computational analysis. Figure 7 shows a total temperature contour and shows that the flame was sustained in the step region and not the cavity.

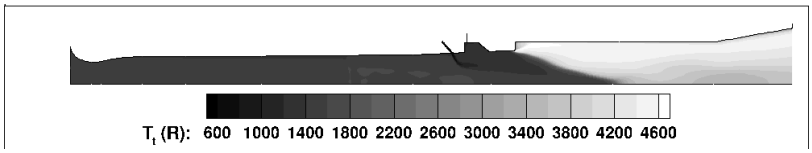

Figure 7. Total temperature contour for case F09175AD

Case F09246AE operated with similar conditions as case F09175AD except this case used the fully divergent configuration and partitioned a portion of its fuel to cavity injection. With the aid of cavity fueling, this case did not predict lean-cavity blowout and it had reasonable shock position and peak pressure predictions, although pressures downstream of the cavity were underestimated. Figure 8 shows wall pressure and contours of pressure and total temperature.

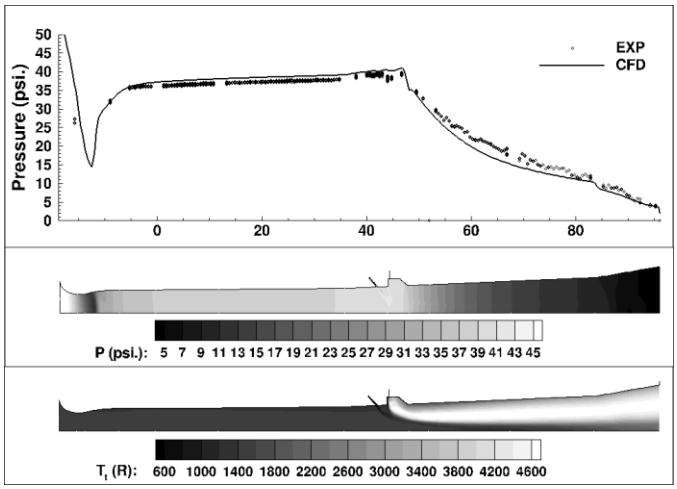

Figure 8. Wall pressure, pressure contour, and total temperature contour for case F09246AE

The baseline results for the twelve cases show a need for improvement when comparing several key parameters to the experiment. Most cases appear to suffer from too much upstream heat release which causes several parameters to become over-predicted. Computationally, case F09175AD suggests that too much upstream heat release caused a decoupling effect between the fuel stream and the cavity which caused premature lean-cavity blowout. Case F09246AE showed that cavity assisted fueling aided in preventing lean-cavity blowout. Three possible deficiencies in the computational analysis were examined to test sensitivity and improve the poor baseline predictions. Those deficiencies are air-fuel mixing, kinetics rates, and grid resolution.

VI. Convergence, Grid Resolution, and Periodic Results

Convergence

Typical reacting flow results using the baseline grid and a constant CFL=5.0 required approximately 20,000 to 30,000 iterations to obtain convergence. The formulation of the convergence criterion is described below. Equation 9 is the sum of the mass flow that is entering the domain from the inflow boundaries and is used as the normalization factor in Equation 10. The convergence criterion in Equation 10 is expressed as a normalized-error-in-mass-flow rate, $\dot{m}_e$. In some instances a periodic solution was encountered. Determining convergence of a result that is oscillating between two distinct solutions is shown in Equation 11; the sum of $\dot{m}_e$ for every iteration (k) throughout the entire period of oscillation is divided by the total number of iterations (N) in that period. This produces a mean-normalized-error-in-mass-flow rate, $\bar{\dot{m}}_e$. A later section discusses differences between periodic solutions that were averaged using either a constant CFL or time step.

$$\dot{m}_{in} = \dot{m}_{air} + \dot{m}_{fuel} \quad [9]$$

$$\dot{m}_e = \frac{\dot{m}_{in} - \dot{m}_{out}}{\dot{m}_{in}} \quad [10]$$

$$\bar{\dot{m}}_e = \frac{\sum_k^N \dot{m}_e}{N} \quad [11]$$

The convergence criterion for a result was obtained when the errors in $\bar{\dot{m}}_e$ or $\dot{m}_e$ were less than ± 0.0020. For periodic results, several periods of oscillation were evaluated to determine whether the convergence criterion had been met. The determination of this criterion was based upon the results of case F09175AK. This case demonstrated unique behavior and took twice as long to converge as other cases. Figure 9 shows $\dot{m}_e \times 100\%$ for this case.

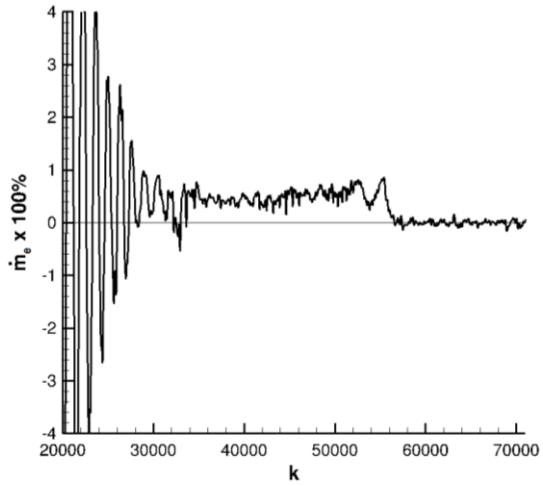

Figure 9: Percentage of the normalized-error-in-mass-flow rate

The kinetics mechanism was initiated at iteration number 11,000 and the solution was expected to converge at iteration number 31,000. Instead, the normalized-error-in-mass-flow rate steadied at +0.5% from iteration numbers ~31,000 -to- ~56,000. Figure 10 shows that pressure in the constant-area section of the combustor at iteration number 41,000 and 51,000 was monotonically decreasing. At iteration number ~56,000 $\dot{m}_e$ began decreasing; results at iteration numbers 61,000 and 71,000 showed no further changes in the predicted wall pressure. The error-in-mass flow from iteration 61,000 and 71,000 fluctuated between ± 0.2%, which thus becomes the criterion for convergence in this study.

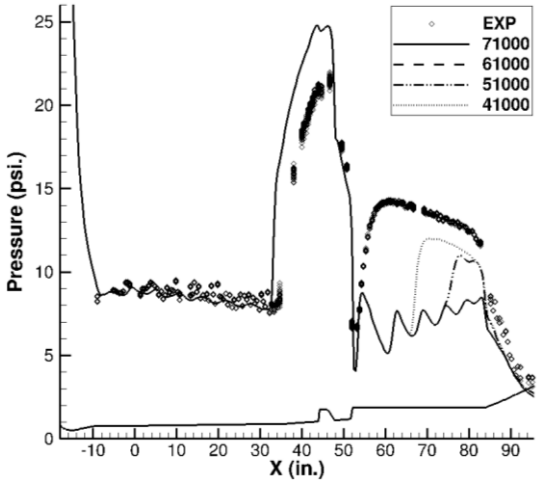

Figure 10: Wall pressure distribution

Figure 11 shows 1D-total temperature. These results suggest that the reacting flow downstream of the step in the constant area section of the combustor at convergence (71,000 iterations) was not releasing enough heat to predict the experimental pressure distribution. (Note: In this study, all predicted 1D-total temperature results were extracted from the CFD using a separated-flow-average utility).[13] Most of the burning and heat release occurred in the cavity flame-holder, where total temperature initially increases, at x = 45-in. There are several reasons for the lack of heat release in the constant-area section of the combustor for the steady state CFD result; one of those reasons is grid resolution, which is discussed in the next section.

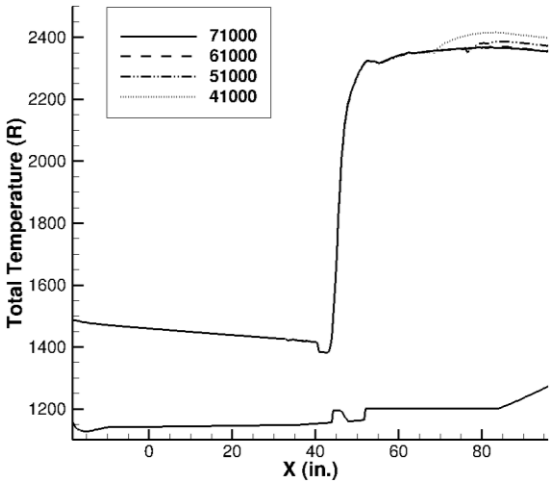

Figure 11: Total temperature

Grid Resolution

In addition to the baseline grid ("baseline"), three additional grids were examined using case F09175AK: Two structured grids and one unstructured. This section observes differences between predictions on grids with varying strategies for refinement. They test the sensitivity of results from the "baseline." As shown in a previous section, the "baseline" for case F09175AK was incapable of predicting the secondary pressure rise in the constant area section of the combustor. The goal in this section is to determine if the lack of secondary pressure rise is due to a lack of grid resolution. 2x and 4x refers to an increase in the number of nodes that occupy a "baseline" grid cell; for instance, 4x, X-dir., means there were 4 times the number of nodes added in the axial direction of the flow which effectively breaks up an individual cell into 4 more cells in the X-direction relative to the baseline. Another example is 4x, XRθ-dir. which means 4 times the number of nodes were applied relative to the baseline in all 3 directions of the flow, thus increasing the total number of cells to 64 cells that occupy the same volume as a baseline grid cell. Table 5 outlines these details regarding each grid type, including the "baseline."

Table 5: Grid information, including resolution and Y+

Grid "name"	Grid Type	Wall Strategy	Y+ (maximum)	Type of Refinement	# of Cells	Step Refinement	Cavity Refinement
baseline	Structured	Function	38	Baseline	2,200,000	Baseline	Baseline
global	Structured	Integration	< 1.0	Global	22,000,000	2x, Xθ-dir. 2.5x, R-dir.	2x, Xθ-dir. 2.5x, R-dir
local	Structured	Function	38	Local	3,340,000	4x, X-dir.	Baseline
unstructured	Unstructured	Function	80	Local	6,620,000	4x, XRθ dir.	4x, XRθ -dir.

The "global" grid was globally refined, which means that the number of nodes in the axial and circumferential direction was doubled (2x). The radial direction (wall normal) was increased by a factor of 2.5x and incorporated a redistribution of nodes to provide integration of the boundary layer (initial wall spacing was 0.0001-in.).

The "local" grid was locally refined in the combustor section C3 by a factor of 4x in the X-direction only. The cavity region and all other regions kept the "baseline" node distributions and cell sizes.

The "unstructured" grid was constructed using Metacomp's unstructured mesh generation software, MIME.[9] The grid used prism layers near wall regions and filled the remaining volume with tetrahedrals. The grid was constructed in a way that maintained similar cell volumes as the "baseline," but the level of refinement used for the step region was also used in the cavity region. The length of one side of a tetrahedral in the step region was equivalent to length of the streamwise side (X-direction) of a hexahedral from the step region of the "local" grid. A density clustering utility from MIME was used for the refinement of the cavity and a portion of the step region. Initial wall spacing was accidentally set to 0.004-in. for the "unstructured" grid whereas the baseline value was 0.002-in. This is why Y+ values were doubled, but the discrepancy proved inconsequential after a boundary layer assessment. The left section of Figure 12 shows the location where local refinement was implemented in the

geometry (Note: For the unstructured grid, local refinement was also used in the cavity region); on the right, a close-up view of the step region is shown for each grid type. Figure 13 shows wall pressure for each grid.

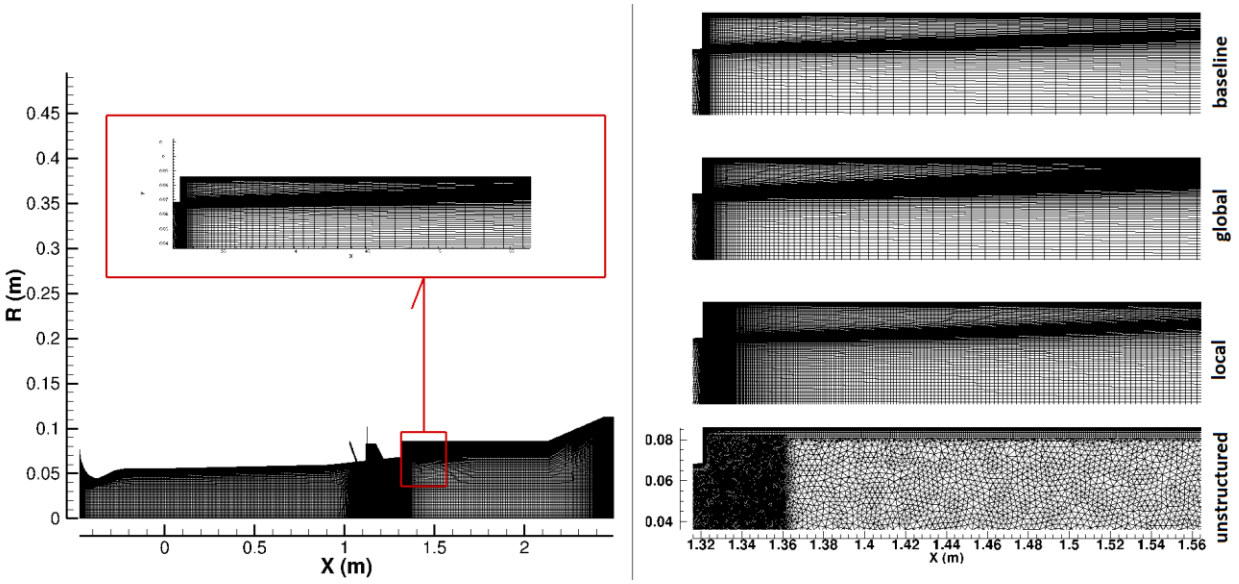

Figure 12: Grid refinement location and views of all 4 grids

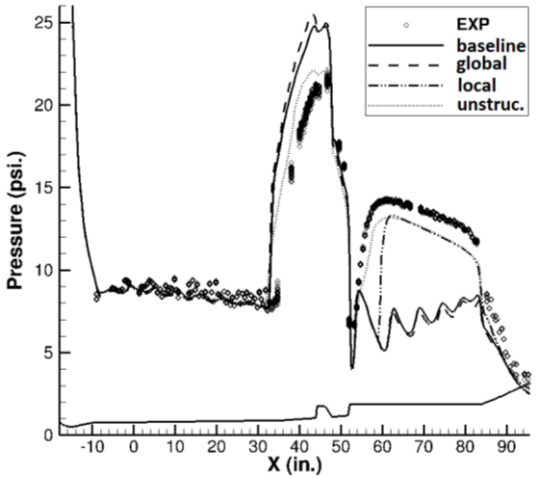

Figure 13: Wall pressure for all 4 grid types

The result on "global" predicted a wall pressure distribution that was very similar to the solution obtained from the "baseline." Shock position was identical and neither predicted the secondary pressure rise in the constant area section of the combustor. The "local" result was capable of predicting the secondary pressure rise in the constant area section of the combustor. The "unstructured" result produced a pressure distribution nearly identical to the experiment and predicted a peak pressure that was 12% (3-psi.) less than the baseline predicted result. All predicted the same isolator shock position. Figure 14 shows static-temperature contour and OH-mass-fraction contour along the centerline of the primary injector. For the "unstructured," notice that both temperature and OH levels are lower in the cavity and greater further downstream, especially behind the step in the constant-area section of the combustor. The "local" shows a decoupled flame region behind the step and "unstructured" shows a fully coupled flame region. The "baseline" and "global" show lower levels of OH and static temperature in the step region. Figure 15 shows the remaining parameters by which each was evaluated.

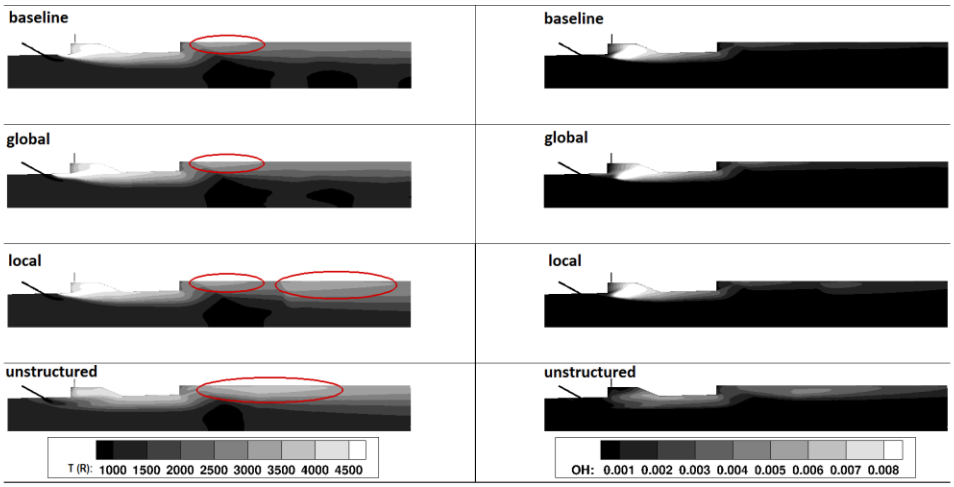

Figure 14: Temperature contour (left) and mass fraction of OH contour (right)

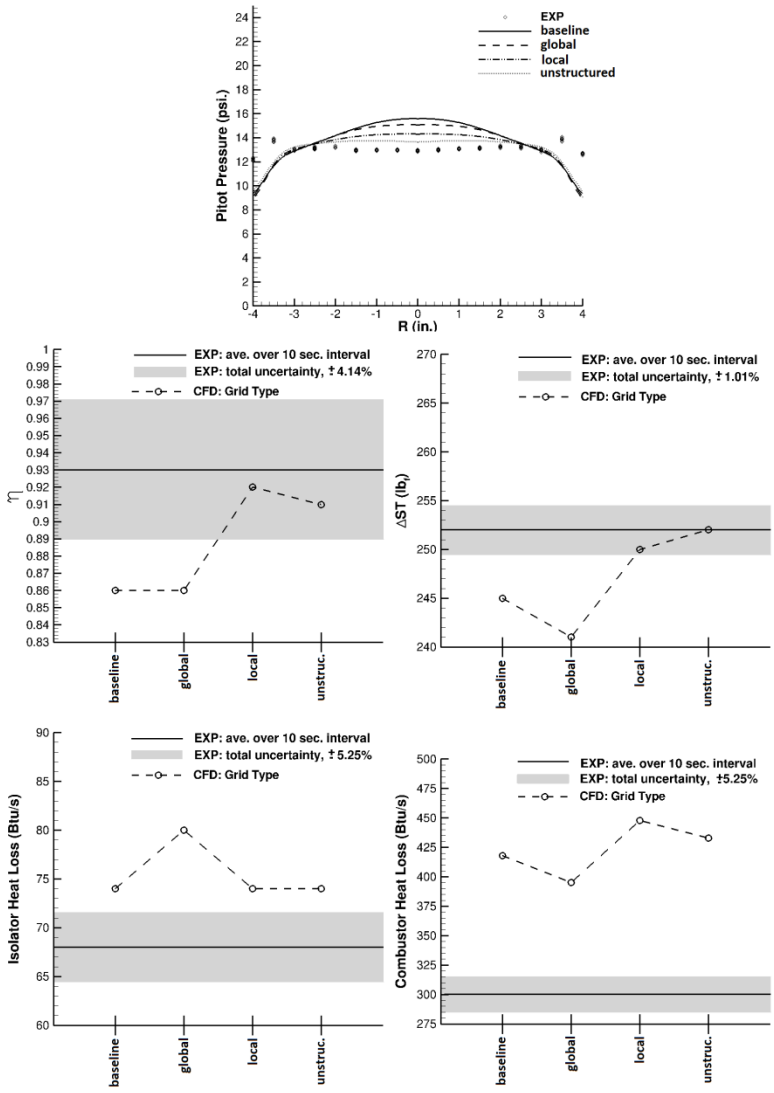

Figure 15: Pitot pressure, performance, and heat transfer

The combustor-exit-Pitot pressure predictions (top) improved with increased grid resolution and the "unstructured" had the best agreement with the experiment. Combustion efficiency fell within the range of experimental uncertainty for both the "local" and "unstructured" (middle left). The "local" and "unstructured" produced values within the range of experimental uncertainty for Δ-stream thrust, with the "unstructured" exactly matching the experimental result; the predictions on the other two grid types under-predicted Δ-stream thrust. The "baseline", "local", and "unstructured" all maintained the same refinement in the isolator and all predicted the same isolator heat loss (bottom left). The "global" used boundary layer integration and predicted slightly different levels of isolator and combustor heat loss, but the differences were negligible and generally did not significantly improve the analysis. All combustor heat loss predictions were over-predicted by at least 32%. Figure 16 shows an in-stream distribution of velocity at the entrance to the isolator (X=0.0-in.). It shows negligible differences between resolved boundary layers that used wall functions or wall integration. The boundary layer is approximately 0.31-in. thick, which is 14% of the duct radius.

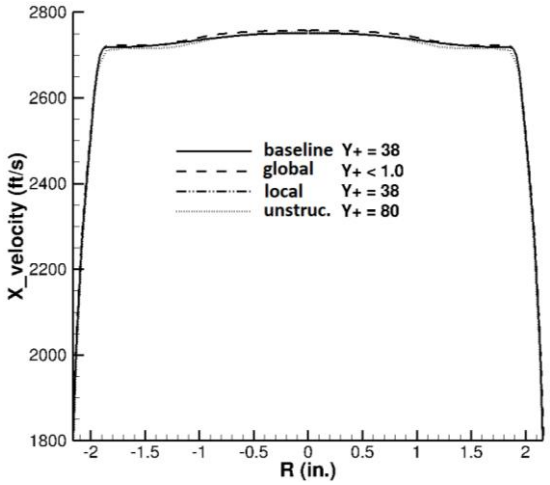

Figure 16: In-stream velocity profile at isolator entrance

The inviscid component of stream thrust is calculated experimentally using wall pressure and area ($\int P * dA$), but the viscous component is determined by subtracting the wall pressure integral and the injector momentum force from the load cell derived Δ-stream thrust. The CFD calculates both the inviscid and viscous components of stream thrust. Table 6 shows components of Δ-stream thrust for both the experiment and the CFD. In terms of a sum of forces, Δ-stream thrust is equal to the inviscid forces subtracted by the viscous forces.

Table 6: Summary of Inviscid Force

Δ-Inviscid Force (lb_f)	I1+I2+C1+C2	C3+C4+C5	Total
baseline	145	170	315
global	144	167	311
local	144	170	314
unstructured	129	180	309
exp.	--	--	362 (measured)

Table 7: Summary of Viscous Force

Δ-Viscous Force (lb_f)	I1+I2+C1+C2	C3+C4+C5	Total
baseline	31	39	70
Global	32	38	70
Local	31	33	64
Unstructured	32	25	57
exp.	--	--	110 (deduced)

The CFD under-predicts both the inviscid and viscous components of Δ-stream thrust, but it appears that the errors in the components cancel out and the predicted Δ-stream thrust ends up in good agreement with the experiment (recall Figure 15). The first column (I1+I2+C1+C2) from Table 6 shows a 16-lb_f decrease in force from

the "unstructured" as compared to the "baseline." This was due to the decreased peak pressure. The second column (C3+C4+C5) shows a 10-lb_f increase in the inviscid force. This is because of increased pressure acting on the backward facing step portion of the combustor; any pressure force acting on this step acts parallel to the flow, which results in increased thrust. The "local" predicted a secondary pressure rise in the constant area section of the combustor, but this pressure rise acted further downstream of the step so no net increase in pressure force was detected on the step face; therefore, any increased pressure force in the constant area section acted perpendicular to the flow and resulted in a zero net increase in thrust. Figure 17 shows contours of pressure acting on the backward facing step of the combustor for the "baseline", "local," and "unstructured." The area of the step face is 13.3-in^2. If one takes the difference in pressure on the step surface from the "unstructured" and the "baseline," which is 0.77-psia and then multiplies it by the area of the step face (13.3-in^2), the additional force acting on the step for the "unstructured" is equivalent to 10-lb_f. This is why the "unstructured" had a 10-lb_f increase in the inviscid component of thrust in sections C3+C4+C5 relative to the "baseline" (recall Table 6). There was also a 14-lb_f decrease in the viscous component of force between the "baseline" and "unstructured," as seen in Table 7, column C3+C4+C5.

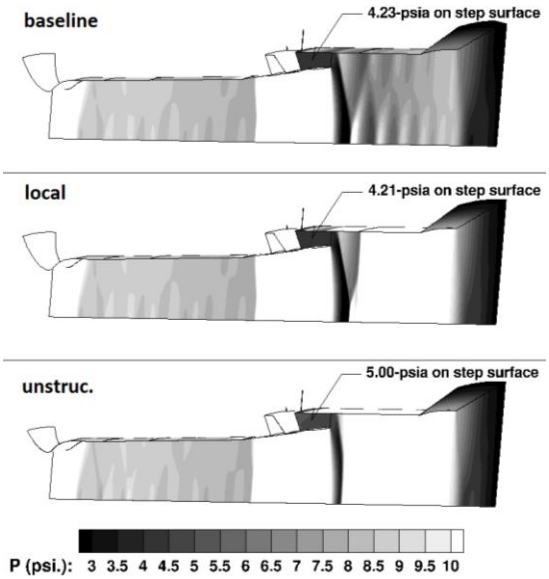

Figure 17: 3D-pressure contours

The "baseline" was the most computationally efficient and was capable of producing a solution in 1 week (wall-time) using 128 processors. The "global" "local" and "unstructured" took 8, 1.5, and 3 weeks, respectively, this also includes average queue time. It was decided to perform further investigations using the baseline grid. Future efforts, however, will further investigate the advantages of local refinement for both unstructured and structured grids. The results shown in this section suggest that local refinement in the streamwise direction around regions with chemical reactions improved predictions. The "global" was computationally expensive and effectively yielded the same results as those obtained from the "baseline." Based upon the results from the "baseline" and the "global" it appears that the use of wall functions are acceptable when performing this kind of scramjet analysis.

Periodic Solution Analysis

The baseline computational results in this analysis used a constant Courant–Friedrichs–Lewy (CFL) number, CFL = 5. Case F09175AK using a CFL = 1 was performed to test sensitivity to CFL number. The result using a CFL = 1 was identical to the result produced using a CFL = 5. Another result using a CFL = 10 was performed, but this case predicted a peak pressure that was 5% lower than the case which used the CFL = 5. The maximum CFL number that could be used to perform analysis without overstepping the kinetics model was a CFL = 5.

Mentioned previously was the occurrence of periodic results. This section shows a method that was used for handling computational results that were periodic. It is common to use a constant CFL number when performing steady state RANS analysis. The CFL number is equal to velocity multiplied by the change in time step divided by the change in the length interval which is based on the grid cell size. In this analysis grid sizes were not all the

same, therefore to maintain a constant CFL the time step for each grid cell was different. This means that each computed result for each grid cell is at a different time from one cell to another. This is satisfactory for steady state analysis, because at steady state the result does not change with time. For periodic solutions it is not recommended since the results are skewed by the differences in time between adjacent grid cells. The usual procedure is to switch from a constant CFL to a constant time step for periodic results. This guarantees that all computed results for each grid cell are progressing at the same time. This is why all instantaneous (transient) solutions must be shown using a constant time step and not a constant CFL. In this analysis and with chemical reactions it was computationally expensive to switch to a constant time step since the time step had to be very small to satisfy solution stability.

An averaging technique was used which averaged the solutions from every iteration throughout the entire period of oscillation using a constant CFL. This result was then compared to a periodic solution that was averaged using a constant time step. The results shown in this section were oscillating around convergence (steady state). Two requirements must occur to use the constant CFL-averaging method. First, a clear period of oscillation must be observed. Second, the normalized-error-in-mass-flow rate must satisfy the convergence criteria for the analysis. If these two conditions are satisfied then the result stemming from the CFL-averaging method can be used. This method is of interest since many results with chemical reactions (such as those in this analysis) tend to be unsteady and require averaging. Figure 18 shows mass conservation for case F09175AF, which was chosen for this analysis because of its periodic characteristics.

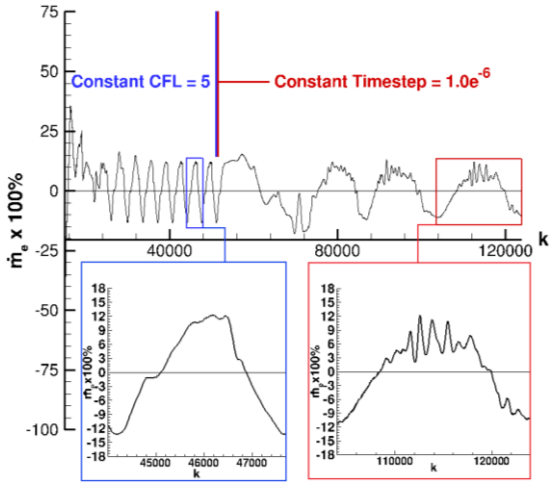

Figure 18: Normalized-error-in-mass-flow rate; periodic solution averaging analysis

The normalized-error-in-mass-flow rate from Figure 18 clearly shows a period of oscillation for the case which used a constant CFL and the case which used a constant time step. The mean-error-in-mass-flow rate fell within the convergence criteria. $\bar{\dot{m}}_e \times 100\%$, for each period, was equal to 0.17%, which satisfies the criteria for convergence. A single time step was used for the constant time step analysis; any time step greater than $1e^{-6}$-sec. resulted in the solution becoming unstable. The wall-time required to complete one-iteration using 128 processors was 6.5-sec for either result using a constant CFL or a constant time step. The periodic result that was produced using a constant CFL spanned 3,700-iterations. The periodic result using a constant time step spanned 20,000 iterations; at a time step of $1e^{-6}$-sec this was equivalent to 0.020-sec or the period repeated itself every 20-millisec. The constant CFL approach, therefore, was 5.4 times more efficient at producing a periodic result. Figure 19 shows wall pressure and contours, Figure 20 shows Pitot pressure, and Figure 21 shows temperature and OH-mass fraction contours.

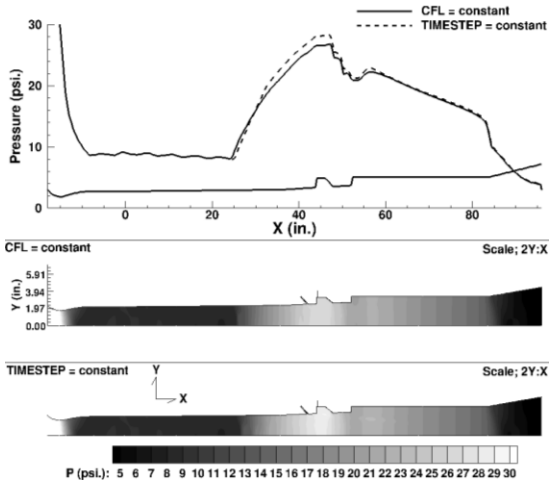

Figure 19: Wall pressure and contours; periodic solution averaging analysis

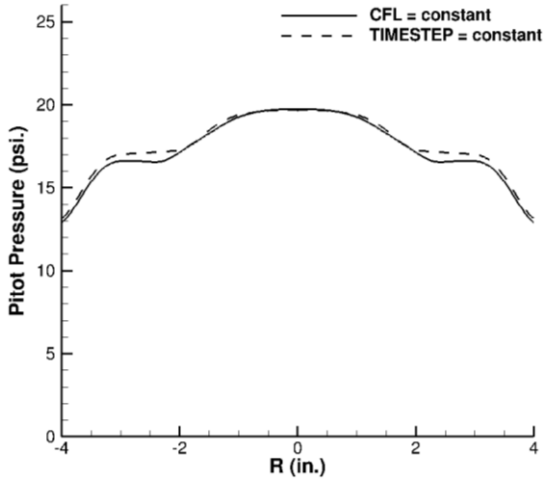

Figure 20: Pitot pressure; periodic solution averaging analysis

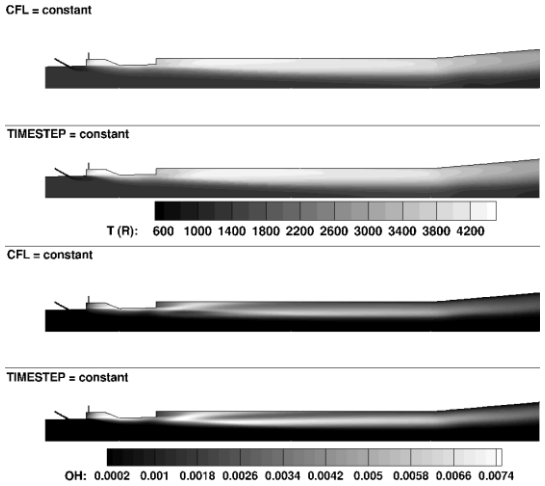

Figure 21: Temperature and OH-mass fraction contours; periodic solution averaging analysis

The case with results averaged using a constant time step predicted a peak pressure that was 1.6-psia greater than the case which used the CFL-averaged result. Shock position is identical between the two cases. Contours of pressure in the flow-field along the primary injector centerline confirm the similarities between the two cases in

terms of combustor pressure distribution. Core Pitot pressure shows that the two cases predicted the same pressure and that the overall distribution is similar. Contours of static temperature and OH further confirm similarities in the flow-field between the two cases. The predicted Δ-stream thrust, combustion efficiency, isolator-heat loss, and combustor-heat loss were [547, 532]-lb_f, [0.74, 0.73], [81, 80]-Btu/s, and [586, 569]-Btu/s for the cases that averaged results using the constant time step and constant CFL, respectively.

The overall analysis saw little impact between results that used either a constant time step or CFL averaging approach. The constant time step approach also proved computationally more expensive. The flow-field features do not appear skewed by the use of the CFL-averaged result. For this type of analysis it was deemed acceptable to use the CFL-averaged result given its computational efficiency and its negligible impact on its average relative to the constant time step average.

VII. Solution Sensitivity Results

Turbulent Schmidt Number Analysis

Case "F09175AK" was used to study the effect of a constant value of turbulent Schmidt number (Sc_T). Figure 22 shows the wall pressure comparison with the experiment using three values for turbulent Schmidt number. The first value of 0.5 was the baseline value; other values were 1.0 and 1.5.

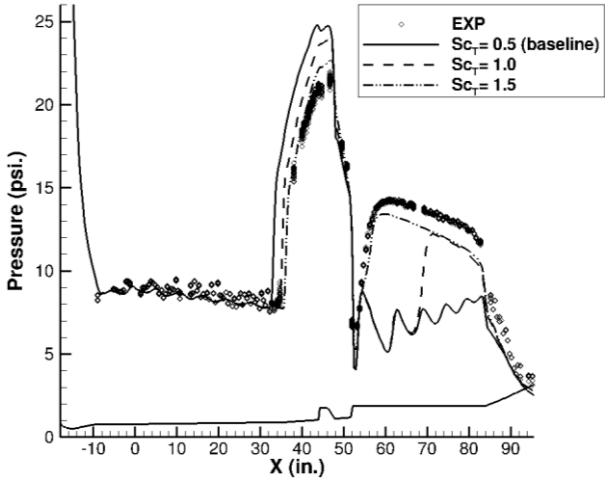

Figure 22: Wall pressure; turbulent Schmidt number analysis

The agreement with the experiment improved as turbulent Schmidt number was increased. As Schmidt number increased by 0.5 the peak combustor pressure decreased by ~1-psia, as compared to the baseline computational result. Shock position only moved 2-in. and 1-in. downstream for Sc_T=1.0 and 1.5, respectively. The movement was small and became smaller at a Sc_T=1.5. It appears that the shock which rested very near the primary flame region (cavity) is moderately insensitive to changes in Schmidt number from 0.5 to 1.5, but this may not be the case at higher equivalence ratios with a shock that rests further upstream in the isolator. Despite the relatively insensitive movement of shock position, changes in Sc_T had a significant impact on the secondary pressure rise downstream of the step in the constant-area section of the combustor. The secondary pressure rise was not predicted at all using the baseline Schmidt number, but with Sc_T=1.0 and 1.5 the secondary pressure rise was predicted and moved upstream by 12-in. Using a Schmidt number of 1.5 provided the best prediction as compared to the experiment. Shown in Figure 23 is 1D-total temperature which depicts additional heat release in the constant area section of the combustor as Sc_T increased.

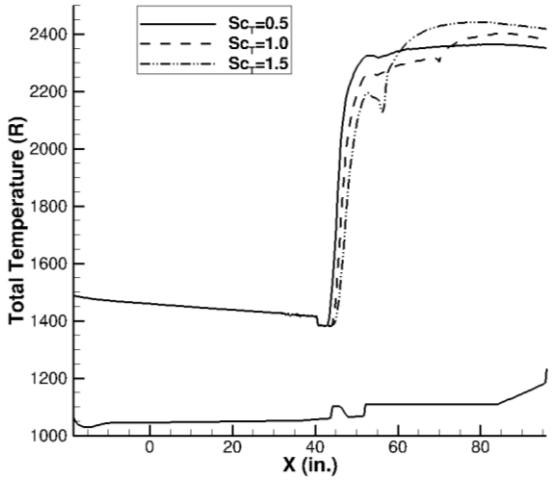

Figure 23: 1D-total temperature; turbulent Schmidt number analysis

Increases in turbulent Schmidt number also influenced the combustor-exit-Pitot pressure comparison with the experiment. The computation over-predicted core Pitot pressure by 2.7-psia (21%) with Sc_T=0.5. Using a Sc_T=1.5, the CFD only over-predicted the experiment by 1.6-psia (12.5%). The experiment showed uniform Pitot pressure at the combustor exit and the predicted Pitot pressure became more uniform with increasing Schmidt number, as shown in Figure 24. The prediction shows that increased core-total temperature correlates with decreased core-Mach number (Rayleigh flow) which resulted in a more uniform Pitot distribution, as shown in Figure 25. The difference in core-total temperature and Mach number between Sc_T=0.5 and Sc_T=1.5 was 100-R and 0.17, respectively.

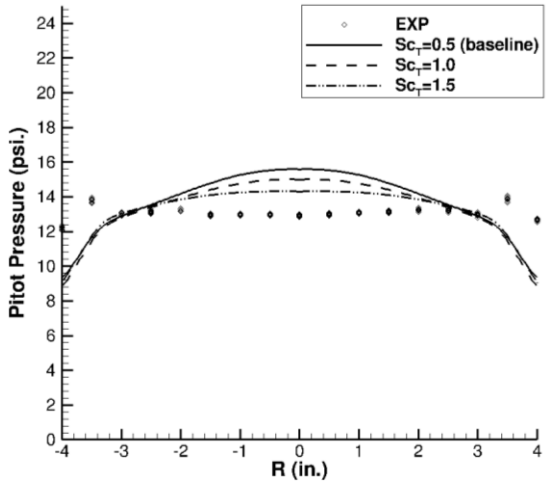

Figure 24: Pitot pressure; turbulent Schmidt number analysis

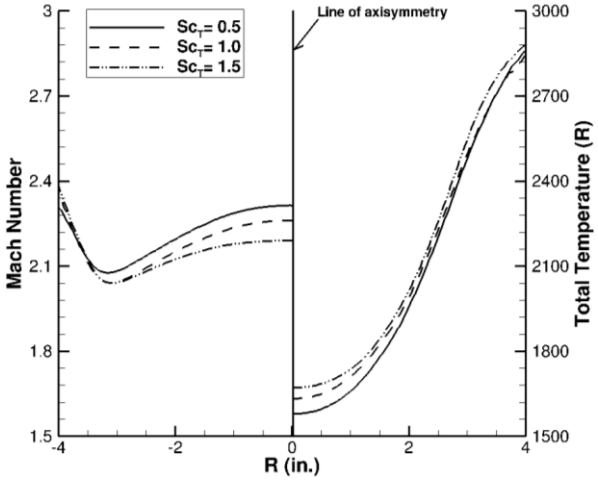

Figure 25: Mach number and total temperature; turbulent Schmidt number analysis

The performance comparisons with the experiment also improved as Schmidt number was increased to 1.5. The predicted Δ-stream thrust and combustion efficiency both fell within the range of experimental uncertainty when Schmidt number was increased to 1.5. Figure 26 shows Δ-stream thrust. Figure 27 shows combustion efficiency.

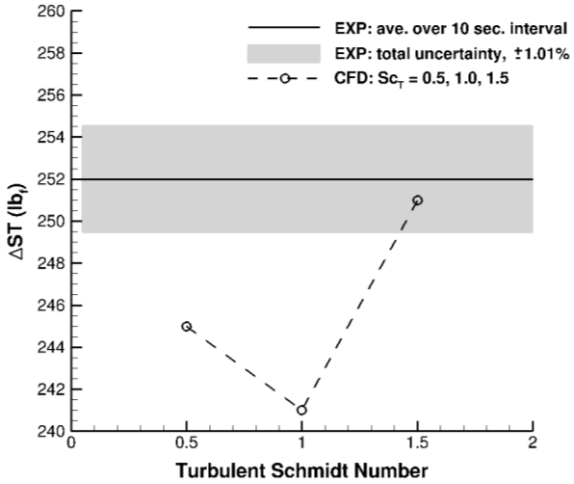

Figure 26: Δ-Stream thrust; turbulent Schmidt number analysis

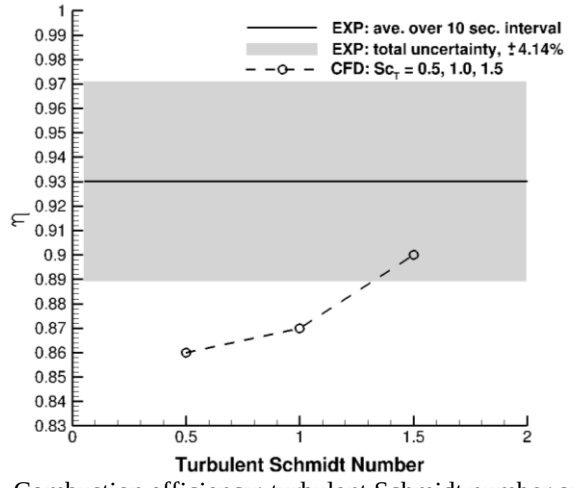

Figure 27: Combustion efficiency; turbulent Schmidt number analysis

Using Sc_T=1.0 resulted in reduced peak pressure and caused a small 4-lb_f decrease in Δ-stream thrust as compared to the baseline. As combustion shifted downstream, the secondary pressure rise in the constant area section of the combustor downstream of the step did not contribute to any increase in Δ-stream thrust. Sc_T=1.5 yielded a higher pressure on the step portion of the combustor, which resulted in increased Δ-stream thrust. The interaction of the secondary pressure rise and the step in the constant-area section of the combustor and their effects on Δ-stream thrust is identical to the effects shown in the Grid Resolution Study (recall Figure 17). Figure 28 shows a 3D-pressure contour, notice the pressure on the step face. Combustion efficiency increased with increasing Schmidt number because of the additional burning in the constant-area section; Sc_T=1.5 predicted combustion efficiency within the range of experimental uncertainty. It was not expected that combustion efficiency would increase with increasing Schmidt number since this decreases mixing, but for this case a higher Sc_T provided more fuel to burn in the combustion zone behind the step, which effectively increased combustion efficiency.

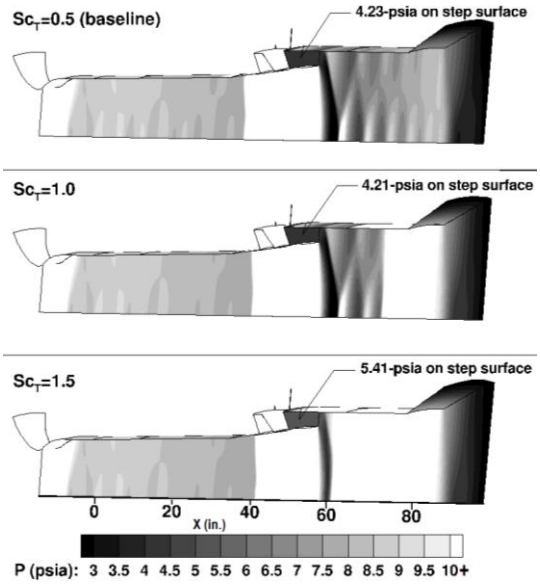

Figure 28: 3D-pressure; turbulent Schmidt number analysis

Shown in Figure 29 are isolator (left) and combustor (right) heat transfer. As the predicted isolator-shock position improved with the experiment so did the isolator-heat transfer. For Sc_T=1.0 and 1.5 the isolator-heat transfer fell within the range of experimental uncertainty, but the CFD did not acceptably predict combustor-heat transfer for any given Schmidt number. The prediction worsened with increased Schmidt number; at Sc_T=1.5, the computation over-predicted the experimental values of combustor-heat transfer by 42%.

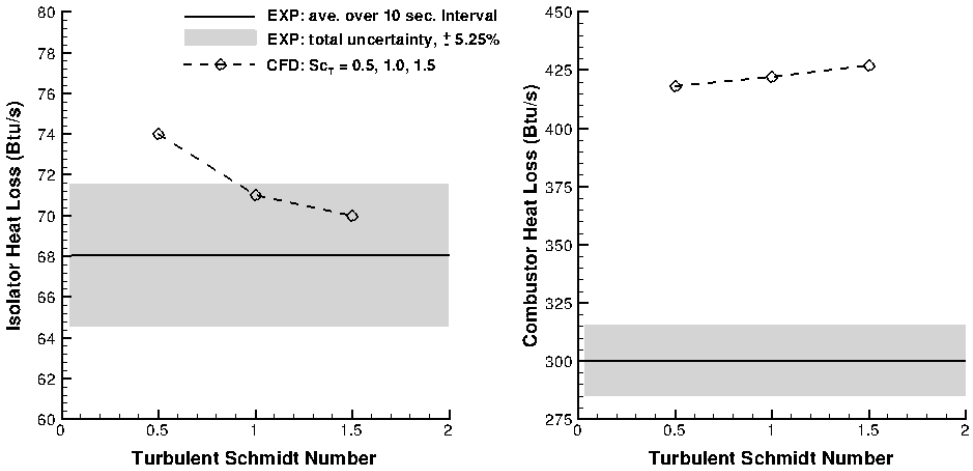

Figure 29: Isolator and combustor heat transfer; turbulent Schmidt number analysis

A variable turbulent Schmidt number model was investigated using case F09175AK. Figure 30 shows the wall pressure predictions for the cases that used the baseline Schmidt number of 0.5 and the case which used the variable Schmidt number, notice negligible differences were observed between the two analyses. Other parameters such as Pitot pressure, performance, and heat transfer also showed negligible differences.

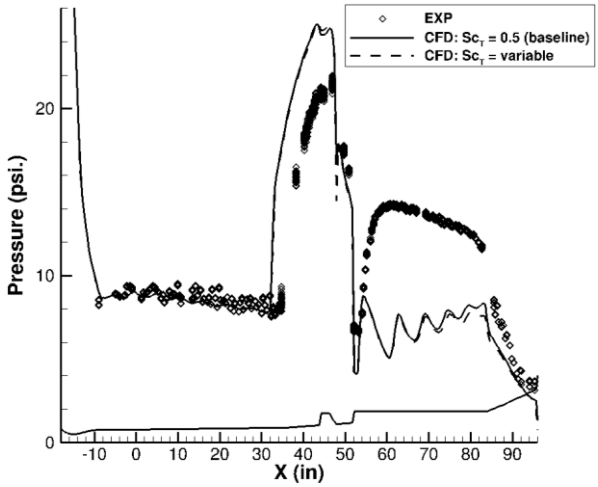

Figure 30: Wall pressure; variable turbulent Schmidt number analysis

Another sensitivity involving the turbulence model was sensitivity to turbulent quantities such as turbulent kinetic energy and its dissipation rate. A wide range of initializations were used on both the nozzle inflow boundary and the injector inflow boundaries for case F09175AK and case F09062BI. The range included quantities that had high levels of turbulence and low levels of dissipation and vice versa. Negligible effects were observed when initializing turbulence differently for these two cases.

Reaction Rate Analysis

In this section a sensitivity study was performed with regard to the finite-chemical-reaction rate of the TP2 kinetics model. The average uncertainty with regard to the reaction rates associated with TP2 is on the order of a factor of ± 2.[11] Case F09175AK was again used in this study and three cases were examined. The first case was the original baseline, which used the original reaction rates as provided by the TP2 developers. The second case reduced all the reaction rates by a factor of two and the third case reduced all rates by a factor of four. All other computational aspects in this study used baseline values and parameters. Figure 31 shows wall pressure for the three reaction rates.

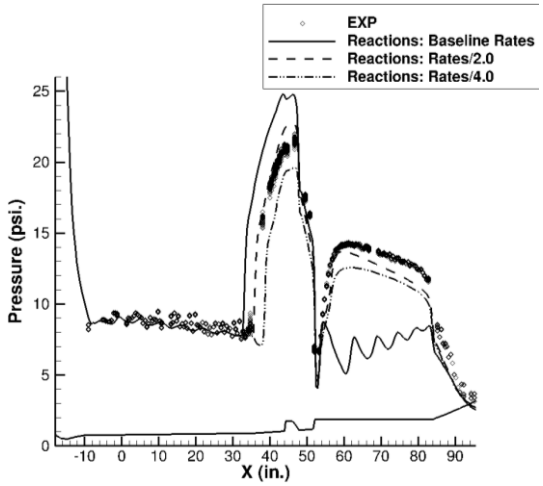

Figure 31: Wall pressure; reaction rate analysis

Slowing down the reaction rates by a factor of two caused the peak combustor pressure and shock position to decrease and move downstream by 2-psia and 3-in., respectively, as compared to the baseline. This resulted in the best comparison with experimental data. The case which reduced rates by a factor of four caused the peak combustor pressure to decrease by 2-psia and shock position to under-predict the experiment by 3-in. Figure 32 shows Pitot pressure.

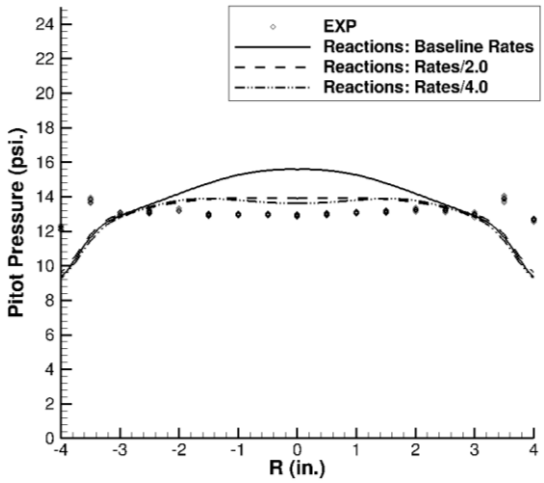

Figure 32: Pitot pressure; reaction rate analysis

The baseline case over-predicted the Pitot pressure by 21%, but with reaction rate reduction the agreement improved significantly. When the rates were reduced by factors of two and four the CFD only over-predicted Pitot pressure by 8% and 5%, respectively. Figure 33 shows the performance evaluation of the reaction rate reduction study and it shows that the predicted performance was either marginally improved or was significantly degraded as compared to the experiment. No level of rate reduction placed the predicted performance within the range of experimental uncertainty. Rates which were cut by a factor of four caused the predicted performance values to significantly deviate from experimentally measured values. Shown in Figure 34, isolator-heat transfer was improved with decreased reaction rate but the combustor-heat transfer remained significantly over-predicted.

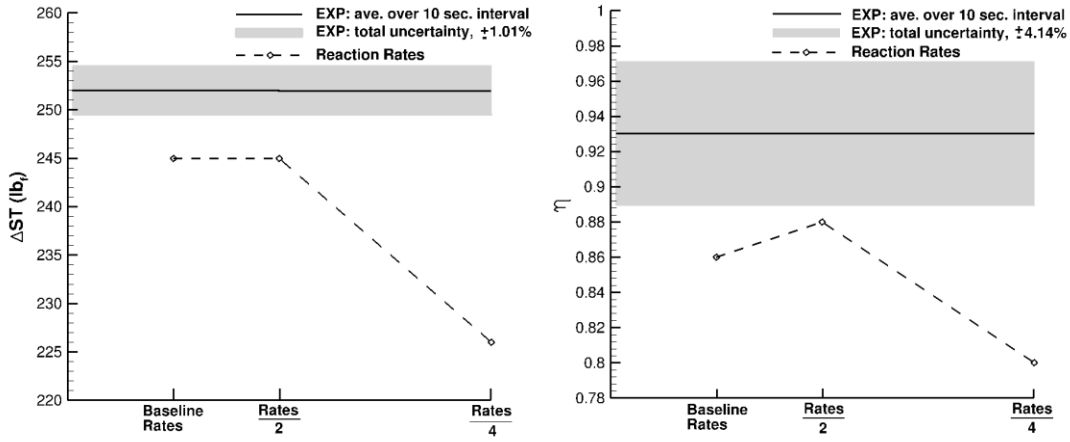

Figure 33: Stream thrust and combustion efficiency; reaction rate analysis

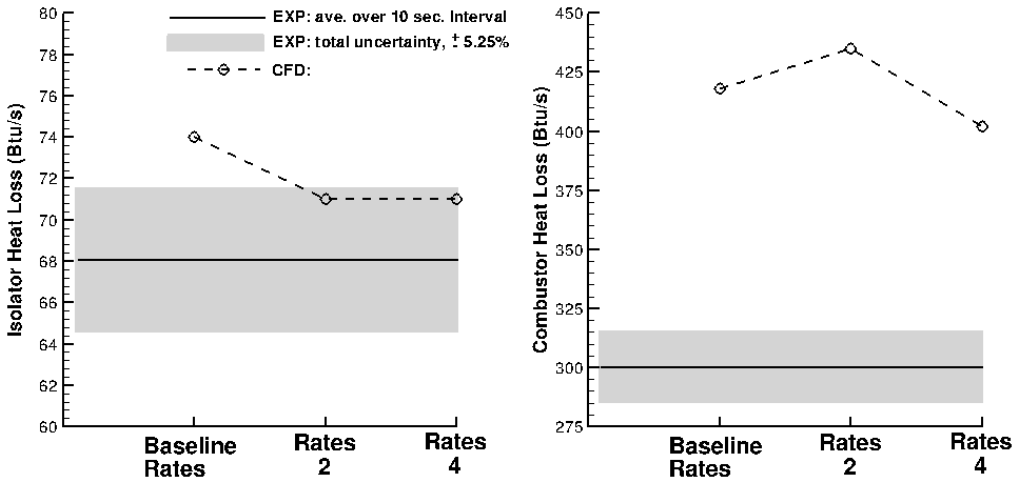

Figure 34: Isolator and combustor heat transfer; reaction rate analysis

Pitot Housing Analysis

Concerns with regard to the accuracy of predictions for Pitot pressure are addressed in this section. This study is a little different than the previous two studies. It is less of a computational sensitivity study and more of a geometry sensitivity study that examines the effect of simplifying a problem by making the assumption that certain aspects to modeling evaluation process are insignificant. In the experiment, the rotating probe ports at the exit of the combustor are placed 2.2-in downstream of the combustor exit with two geometric expansions and an air gap between the probe location and the C5-exit flange. A sensitivity study was performed to determine what impact the wall geometry and the air gap had on the in-stream Pitot measurements. Figure 35 shows a centerline outline of the experimental hardware; on the radial axis (R-in.) the locations of the Pitot probes are outlined; along the x-axis (X-in.) locations are described relative to the isolator entrance; all other dimensions are absolute.

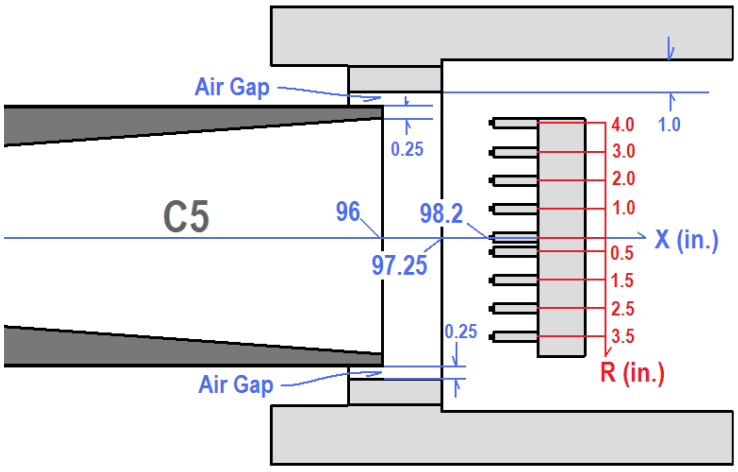

Figure 35: Probe housing geometry (experimental setup)

Two grids were used to determine the effect of the probe geometry. The baseline grid simply modeled the axial location of the Pitot probes but did not model the complex wall expansions. The alternate grid modeled the complex expansions at the combustor exit. Two modeling strategies were employed using the alternate grid; the first modeled the geometry of the expansions inside the probe housing but neglected the effects of the air gap; the second took into account the effects of the air gap by using a backpressure imposed boundary condition. Figure 36 shows an axisymmetric outline of the grids used for modeling of the probe section and includes the boundary conditions used for the different analyses. On the left is the baseline grid which did not include the wall expansions and simply used a centroidal extrapolation boundary condition downstream of the C5 flange (wall). On the right is the alternate grid, which modeled the wall expansions.

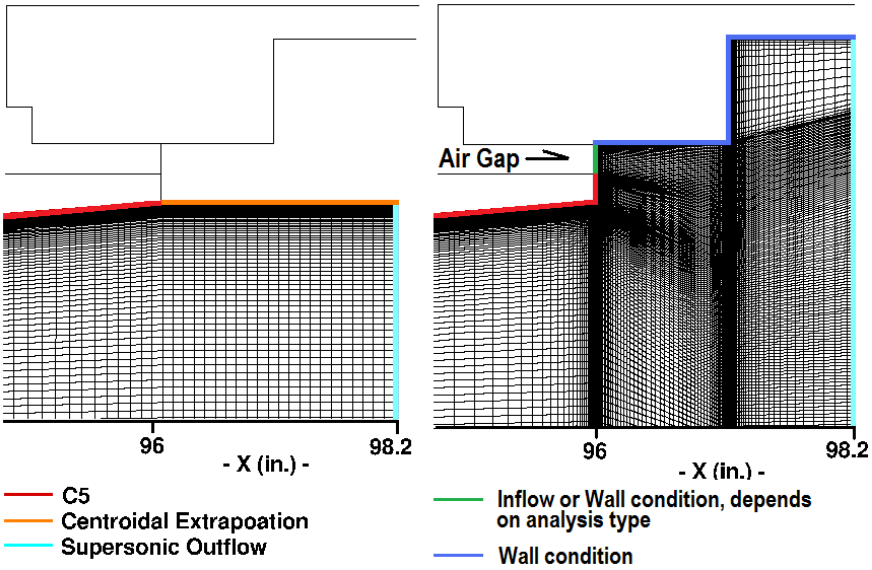

Figure 36: Probe housing grids; baseline (left) and alternate (right)

Computationally, static pressure, Mach number, and gamma were extracted at the supersonic outflow plane and Equation 12 was used to calculate the in-stream-Pitot distribution. Experimentally, Pitot pressure is only measured in the supersonic portions of the flow so the locally computed Mach number in the computations was constrained to values of $M \geq 1$. Figure 37 shows the results for Pitot pressure for the three types of computational analyses as compared to the experiment. The results shown in this section are once again for case F09175AK.

$$P_{o,2} = P\left[\frac{(\gamma+1)^2 M^2}{4\gamma M^2 - 2(\gamma-1)}\right]^{\frac{\gamma}{\gamma-1}} \times \left[\frac{1-\gamma+2\gamma M^2}{\gamma+1}\right], \qquad M \geq 1 \qquad [12]$$

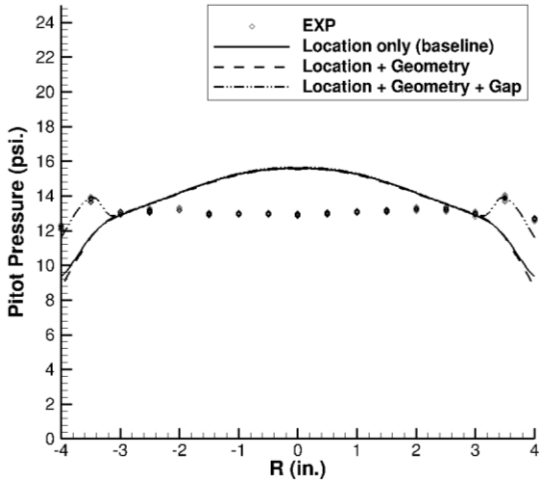

Figure 37: Pitot pressure; Pitot housing analysis

The computation over-predicted the core Pitot pressure as compared to the experiment, but the over-prediction does not appear to be influenced by the wall geometry or the air gap at the combustor exit. The air gap had the greatest impact on the outer-most Pitot measurements and produced two peaks in Pitot pressure, at R = ± 3.5-in. The computational results were able to accurately model the peaks seen in the experimental data by including the additional air coming through the air gap. Computationally, 34.4% air was leaking into the probe housing through the air gap relative to the air supplied to the test section by the facility nozzle.

Equation 13, from classical compressible flow theory which assumes "choked" airflow (M=1), was used to determine if the computationally obtained percentage was reasonable.

$$\dot{m} = A\sqrt{\frac{\gamma}{R}\left(\frac{2}{\gamma+1}\right)^{\frac{\gamma+1}{\gamma-1}}}\frac{P_o}{\sqrt{T_o}} \qquad [13]$$

The area (A) was the area of the air gap, the total pressure (P_o) was atmosphere, the total temperature (T_o) was room temperature, R is the ideal gas constant for air and gamma was assumed to be 1.4. This showed that for "choked" airflow the theoretical mass flow through the air gap was 2.53-lbm/s; when expressed as a percentage of the inflow air from the facility nozzle this equates to 35.6%, thus the computationally computed percentage of mass flow through the air gap (34.4%) was reasonable.

Figure 38 shows a contour of pressure for the three modeling strategies. Shown (top) is the oblique shock caused by the air entering the gap. When compared to the other analyses it does not appear there is any flow separation at the combustor exit (X = 96.0-in). The markings in white are the locations of the Pitot rakes from the experiment. Notice the pressure wave that intersects the end of the Pitot rake (R = 3.5-in), which causes the spikes in Pitot pressure (Figure 37).

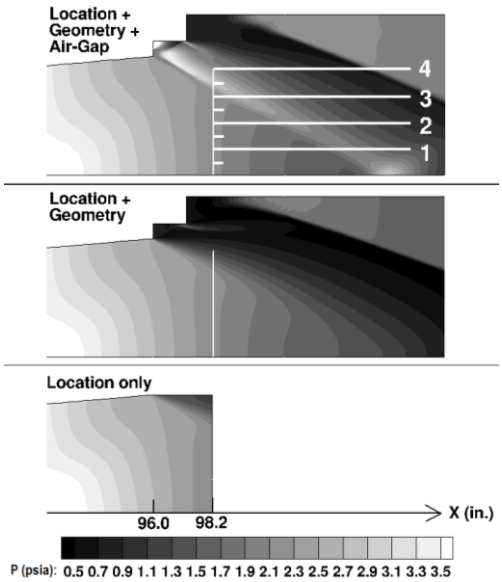

Figure 38: Pressure contours; Pitot housing analysis

Modeling the air-gap and the wall expansions added approximately 1.5 million hexahedral cells to the overall grid (50% increase in the total number of cells). The air gap was found to only effect the comparison of the outer-most Pitot pressures with the experiment; this fact was considered against the computational expense of modeling the wall expansions and it was decided to document the discrepancy in Pitot pressure caused by the air gap and to perform all further analysis using the simpler and more computationally efficient baseline grid which has been used extensively in this analysis.

VIII. Improved Results

In this analysis three methods were found to be capable of improving predicted results versus measured data for case F09175AK. These methods were to calibrate via adjusting the constant value for turbulent Schmidt number, reducing the reaction rates of the kinetics model, and refining the grid in regions with chemical reactions. These methods were therefore applied to two additional cases (F09194AF and F09062BI) in an attempt to observe the spectrum at which these improvements could be effective. This section compares a combination of reaction rate reduction and Schmidt number adjustment versus grid resolution. It was determined that using the baseline grid and a Sc_T=0.7 with the reaction rates reduced by a factor of two was the combination with the most potential to benefit all twelve cases. This determination was made based on results shown in this analysis and other supplemental

analysis. In the supplemental analysis, it was attempted to use a Schmidt number of 1.0 with rates reduced by a factor of two but case F09194AF was highly unsteady and was incapable of producing a "steady" or periodic result. A Sc_T=0.5 with rates reduced by a factor of two had almost no impact on case F09062BI, therefore a Schmidt of 0.7 was chosen because it showed some improvement to case F09062BI.

Case F09175AK has been used extensively throughout most of this analysis and it operated using the M=1.8 nozzle, at a total Φ=0.3 (primary fuel injection only) and used the configuration with the step. Using the baseline grid and baseline numerics this case struggled to predict shock position, peak pressure, downstream pressure, heat loss, and combustor-exit Pitot pressure as compared to the experiment.

Case F09194AF used the same nozzle and combustor configuration as F09175AK, but it operated at a total Φ=0.89 with fuel distributed between the primary and secondary fuel injectors. Computationally, this case exhibited a high degree of periodicity in its result and required CFL-solution averaging. This case's baseline results compared well with experimental data in terms of peak pressure and shock position.

The third case used in this section of the analysis was F09062BI, which operated using the M=2.2 nozzle at Φ=0.9 (primary and secondary fuel injection) and used the fully divergent configuration. This case's baseline results over-predicted shock position and peak pressure by a large margin as compared to the experiment, but the Pitot pressure distribution at the combustor exit was reasonable. Figure 39 shows a prediction summary for the three cases using the two different methods of improvement.

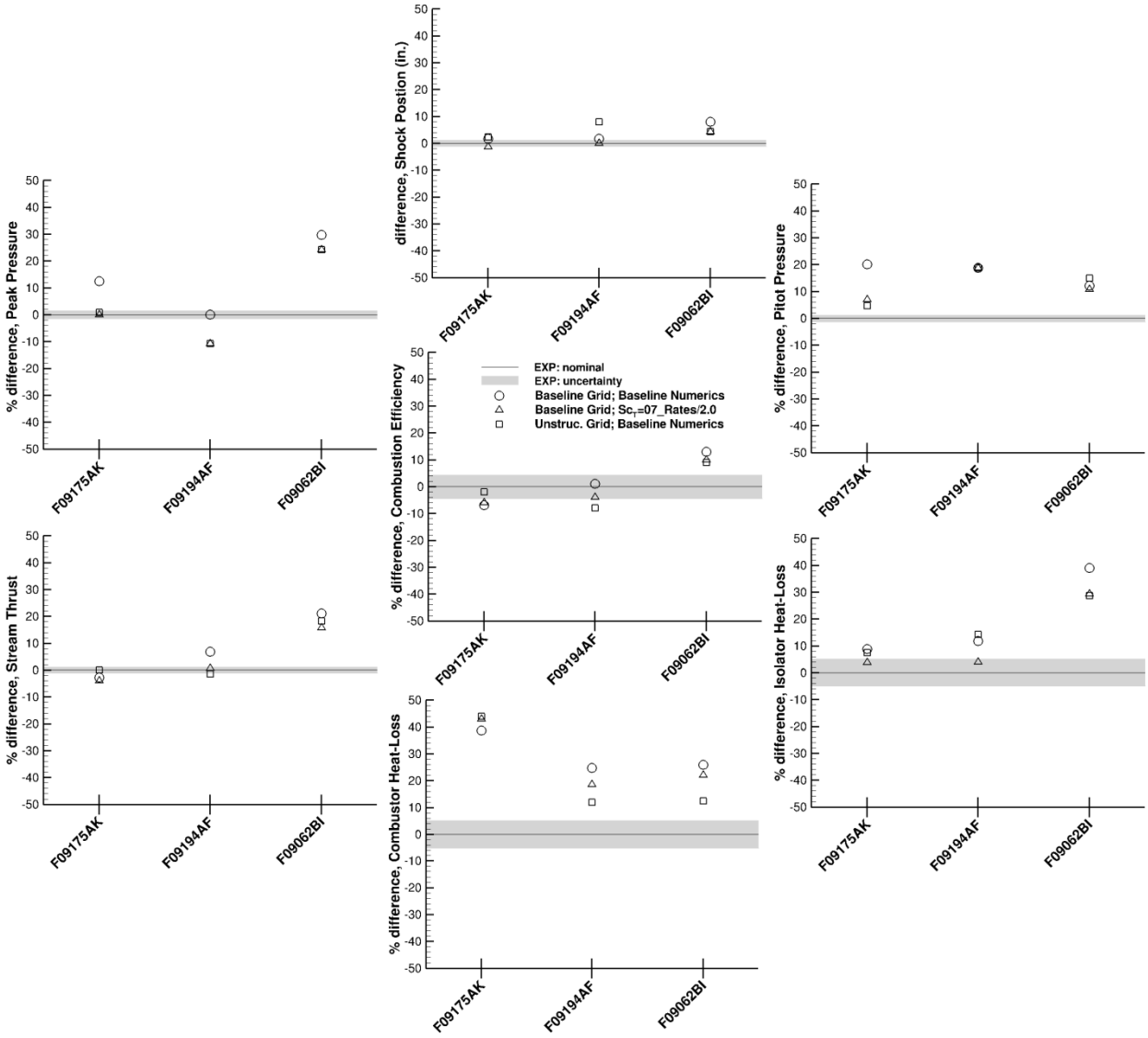

Figure 39: Prediction summary for improved cases

The case using a $Sc_T = 0.7$ with rates cut in half and the case with increased grid resolution significantly improved peak wall pressure and Pitot pressure predictions for case F09175AK. Performance was improved as well, especially for the case using the unstructured grid because it predicted performance within the range of total experimental uncertainty.

The changes to the baseline approach did not improve predictions for case F09194AF. Peak pressure predictions worsened as compared to the baseline, and Pitot pressure was unaffected. Δ-stream thrust predictions improved modestly over the baseline, but the predicted combustion efficiencies worsened. The predicted results for this case also exhibited the highest level of unsteadiness as compared to the other two cases.

Case F09062BI saw slight improvement in its predicted shock position and peak pressure, but Pitot pressure distributions were mostly unaffected. Improvements in the predicted performance were slightly improved as well.

For this data set, Schmidt number and reaction rate adjustment could not improve prediction for all 3 cases. Adjustments to these values improved predictions for two cases but worsened predictions for case F09194AF. Grid refinement also improved prediction for two cases, but worsened prediction for case F09194AF. These results suggest that either method for improvement would improve results for some of the remaining nine cases but would worsen results for other cases. At this point in the analysis it may be infeasible to find a combination of Schmidt number and/or reaction rate that could benefit all twelve cases. Grid independence was not fully justified in this analysis; therefore, further improvements to the grid could potentially improve predictions for all twelve cases. It is important to note that the refined region used in the unstructured grid only extended a few inches downstream of the step. This was sufficient for case F09175AK, which operated at a low Φ with most of its burning occurring near the cavity, but case F09194AF operated at a high Φ and included secondary fuel. This means that most of the burning was occurring downstream of the cavity, outside of the refinement region. A future study may include an extended refinement region, although this will be computationally more expensive.

IX. Conclusions

The goal in this analysis was to improve the predictive capability of the baseline computational analysis with respect to the experiments. This goal was partially achieved for two of the twelve cases but there are still significant modeling challenges in order to achieve broader improvement. The baseline approach used a baseline grid and a set of baseline numerics to achieve the baseline results. Five measured parameters from the experiment were compared to computational results for each of the twelve cases. These parameters were isolator/combustor-wall pressure distribution, combustor-exit-Pitot pressure, Δ-stream thrust, combustion efficiency, and heat loss. Many of the baseline cases over-predicted these parameters because of excessive upstream heat release. Three computational methods for controlling heat release inside a scramjet flow-field were shown to be effective in this analysis. First was grid refinement, second was adjustment to turbulent Schmidt number, and third was adjustment to the reaction rates from the kinetics model.

Grid Resolution Analysis: Case F09175AK

It was shown that a computation performed on a grid which effectively doubled the number of nodes in each coordinate-direction ("global") produced the same result as a computation performed on the "baseline." It was also shown that negligible differences, which includes heat transfer, were observed in computational results that used wall functions up to a $Y+ = 38$ or a computation that integrated the boundary layer with $Y+ \approx 1$.

Locally quadrupling the number of nodes in the axial direction using the "local" grid in the step region of the combustor captured greater heat release as compared to the "baseline." The greater heat release improved predictions.

Quadrupling the number of nodes in each coordinate-direction ("unstructured") in the step region of the combustor effectively captured the same amount of heat release as the computation performed on the "local." Quadrupling the number of nodes in each coordinate-direction in the cavity region captured less heat release relative to the "baseline," which improved the prediction with the experiment.

Results proved highly sensitive to grid refinement in the axial direction of the flow. Results did not appear sensitive to the radial (wall normal) or circumferential directions of the flow. The result performed using the "global" was 8 times more computationally expensive than the "baseline" and did not improve the analysis. Respectively, results obtained using the "local" and "unstructured" were 1.5 and 3 times as expensive as the results obtained using the "baseline" and generally improved the analysis. "Global" refinement proved far too computationally expensive to explore any further, although local refinement in regions with chemical reactions proved promising.

Turbulent Schmidt Number Analysis: Case F09175AK

Using the baseline grid, three turbulent Schmidt numbers were investigated: 0.5, 1.0, and 1.5, with 0.5 being the baseline value. Increasing Schmidt number (reducing mixing) increased combustion efficiency and Δ-stream thrust, which was not expected. Effectively, mixing and burning were reduced in the upstream portion of the combustor near the cavity using Schmidt number = 1.5, which allowed for increased burning in the downstream portion of the combustor near the step region. The increased burning in the step region caused an increase in downstream static pressure. The increase in downstream pressure was realized on the face of the step which ultimately led to increased thrust. All parameters that were compared to the experiment improved with turbulent Schmidt number of 1.5, and many fell within the range of experimental uncertainty. The exception was combustor heat loss. The predicted combustor heat loss worsened with the increased Schmidt number.

A variable turbulent Schmidt number model was also used, and it produced the same predicted results as the baseline result, which did not improve the overall analysis.

Reaction Rate Analysis: Case F09175AK

Using the TP2 chemistry model, reaction rates were reduced by a factor of two and by a factor of four relative to the baseline rates. As in the Schmidt number analysis, combustion was shifted downstream. Downstream heat release was detected in the step region of the combustor. A factor of two reduction improved predictions, but improvements were not as substantial as with Schmidt number adjustment. Also, combustor heat loss prediction worsened with decreased rates. A factor of four reduction in the reaction rates significantly worsened agreement with the experiment by under-predicting results. This proved that a factor of four reduction was too extreme for this case.

Improved Analysis: Case F09175AK, F09194AF, and F09062BI

Computational modifications were extended to two additional cases in this analysis. It was shown that a combination of Schmidt number and reaction rate adjustment improved results for cases F09175AK and F09062BI relative to the baseline Schmidt number and reaction rate. Predictions, however, worsened for case F09194AF. It was also shown that the locally refined unstructured grid improved results for the same two cases, but generally worsened prediction for the other case. It was determined that Schmidt number + reaction rate adjustment or grid refinement could be used for all twelve cases to achieve improved results for some of the cases, but others would be adversely affected. It does not appear any further adjustment to the reaction rates or Schmidt number could improve all twelve cases. Further grid refinement could still improve all twelve cases, but in this analysis it was undetermined that either approach was better than the other.

Other Analysis

It was shown that CFL-averaging a periodic result effectively produced the same result as averaging a periodic result using a constant time step. CFL-averaging a periodic result offered a 5.4 times reduction in computational expense.

Computationally, it was shown that the air gap which is present at the exit of the RC22 combustor can influence the outer-most Pitot measurements. Pitot measurements from 0.0- to 3.0-in. radial are not affected by the air gap. It was also shown that approximately 2.53-lbm/sec. of air was entering through the air gap in simulated Mach 3.5 flight using the M=1.8 facility nozzle.

X. Future Analysis

Making further improvements to the modeling may improve prediction and could potentially benefit all twelve cases. Grid refinement in regions with chemical reactions should further be explored. Other methods such as LES or Hybrid LES/RANS could offer the greatest improvement to the mixing in the modeling although these methods, at the present, are too computationally expensive to perform a broad computational analysis like the analysis performed in this study. Other sensitivities can also be examined such turbulence model, kinetics mechanism, compressibility correction, and others. A great deal of improvement is needed for the heat transfer analysis. Effects such as radiation and water-side-convective-heat transfer need to be explored to possibly improve the heat transfer analysis. RC22 has some data available for cold start operation and ignition. Modeling of cold start could be used

in the future to better understand the phenomena associated with cold start. This would require some retooling of the modeling methods that were used in this analysis and would require the use of a constant time step since the analysis would be transient.

References

1. Gruber, M., Donbar, J., Jackson, K., Mathur, T., Baurle, R., Eklund, D., and Smith, S., "Newly Developed Direct-Connect High-Enthalpy Supersonic Combustion Research Facility," Journal of Propulsion and Power, Vol. 17, No. 6, 2001, pp. 1296-1304.
2. Milligan, R., Eklund, D., Wolff, J. M., Gruber, M., and Mathur, T., "Dual Mode Scramjet Combustor: Analysis of Two Configurations," AIAA-2010-751.
3. Storch, A. M., Bynum, M., Liu, J., and Gruber, M., "Combustor Operability and Performance Verification for HIFIRE Flight 2," AIAA-2011-2249, April 2011.
4. Sturgess, G.J., and McManus, K.R., "Calculations of Turbulent Mass Transport in a Bluff-Body Diffusion-Flame Combustor," AIAA-84-0372.
5. Smith, S., Gruber, M., Steiner, R., Collatz, M., and Mathur, T., "Development and Calibration of an Axisymmetric Direct-Connect Supersonic Combustion Flowpath," AIAA Paper 2009-5035, August 2009.
6. Smith, S., Gruber, M., Mathur, T., Ryman, R., Diemer, J., and Tam, C.J., "Development of a Rotating Probe System for Supersonic Combustion Experiments," AIAA-2009-5034.
7. Smith, S., Schied, A., Eklund, D., Gruber, M., Wilkin, H., and Mathur, T., "Supersonic Combustion Research Laboratory Uncertainty Analysis," AIAA 2008-5065.
8. Billig, F.S., "Research on Supersonic Combustion," Journal of Propulsion and Power, Vol. 9, No. 4, 1993, pp. 499-514.
9. http://www.metacomptech.com, 2009.
10. Goldberg, U., Peroomian, O., Palaniswamy, S., and Chakravarthy, S., "Anisotropic k-ε Model for Adverse Presure Gradient Flow," AIAA-99-0152.
11. Liu, J., Tam, C.J., Lu, T., and Law, C.K., "Simulations of Cavity-Stabilized Flames in Supersonic Flows Using Reduced Chemical Kinetic Mechanisms," AIAA-2006-4862, 2006.
12. Gruber, M., Smith, S., and Mathur, T., "Experimental Characterization of Hydrocarbon-Fueled Axisymmetric Scramjet Combustor Flowpaths," AIAA-2011-2311, April 2011.
13. Hagenmaier, M., and Davis, D. "Scramjet Component Optimization using CFD and Design of Experiments," AIAA-2002-0544, 2002.